ALMA MATER STUDIORUM · UNIVERSITÀ DI BOLOGNA

SCHOOL OF ENGINEERING
- Forlí Campus -

Second Cycle Master's Degree in
Aerospace Engineering
class LM20
Graduation Thesis in: ING-IND/06 - Fluid Dynamics

Numerical investigation of two-dimensional diffusers at low Reynolds numbers

Candidate :
Alex Ravaioli

Supervisor :
Prof. Gabriele Bellani

Session II
Academic Year 2022/2023

Contents

1 Introduction 1

1.1 Aim of the thesis . . . 2
1.2 Thesis outline . . . 4

2 Theoretical background 5

2.1 Diffusers . . . 5
  2.1.1 Influence of inlet and outlet conditions . . . 12
2.2 Governing equations and turbulence modelling . . . 15
  2.2.1 Governing equations and DNS . . . 15
  2.2.2 RANS . . . 17

3 Methodology 27

3.1 Geometric configuration . . . 27
3.2 Mesh independence study . . . 28
3.3 CFD model implementation and boundary conditions . . . 32

4 Results and discussion 37

4.1 Model validation . . . 37
4.2 Diffuser outlet analysis . . . 40
4.3 Turbulence intensity: 10 percent . . . 46
4.4 Turbulence intensity: 3 percent . . . 47
4.5 Turbulence intensity: 0.05 percent . . . 48
4.6 Modified effectiveness . . . 49

5 Conclusions and future work 57
5.1 Conclusions 57
5.2 Future work 59

Bibliography 63

List of Figures

2.1 Examples of the canonical diffuser shapes. Planar diffusers can be considered two-dimensional if the inlet has a large aspect ratio $AS > 1$. 5

2.2 Sketch of boundary layer separation (G. Buresti [4], 2012, p.214). 6

2.3 Geometry of three-dimensional straight-walled diffusers. 9

2.4 Representation of the displacement thickness in an internal flow. 9

2.5 Flow regimes in straight-wall, 2D diffusers, $Re > 10^4$ [2]. . . . 10

2.6 Relationship between flow regime and pressure recovery coefficient (Casey and Robinson [6], 2021, p.231). 12

2.7 Empirical relationship given by Equation 2.25 which defines the value of $Re_{\theta t}$ in the free-stream as function of the turbulence level. 25

3.1 Diffuser and external chamber geometry. 28

3.2 Diffuser geometry and its nomenclature. 29

3.3 C_P series over time with different external chamber sizes, whose length and height are expressed in diffuser inlet widths (W_1). C_{Popt} is the C_P average of the best geometry (70x140). 29

3.4 Relative C_P averages at different external chamber sizes expressed in diffuser inlet widths. C_{Popt} is the C_P average of the best geometry (70x140). 30

3.5 Mesh of the diffuser and external chamber. 30

3.6 Mesh independence study performed on the inlet cell length expressed in diffuser inlet widths (streamwise, x direction, length of the grid cell). 31
3.7 The three different velocity profiles at the diffuser inlet. 35

4.1 Comparison of pressure recovery coefficients between simulations and experimental data [2], varying the divergence angle. $Tu = 2\%$, $B = 0.007$. The green points were deduced from the interpolation curve of $B = 0.015$. The dashed lines represent the angles of the stall regimes as expressed in Figure 2.5: a-a for the Large Transitory stall, b-b for the Fully-Developed two-dimensional stall, c-c for the Jet Flow. 38
4.2 Relative error of the linear interpolation of the pressure recovery coefficients between simulations and experimental data [2], varying the divergence angle. $Tu = 2\%$, $B = 0.007$. The dashed lines represent the angles of the stall regimes as expressed in Figure 2.5: a-a for the Large Transitory stall, b-b for the Fully-Developed two-dimensional stall, c-c for the Jet Flow. 39
4.3 Velocity profiles at the diffuser outlet at the time instant $t = 5.5s$, for the three inlet blockage factors, and $Tu = 10\%$. . . . 42
4.4 Velocity profiles at the diffuser outlet at the time instant $t = 5.5s$, for the three inlet blockage factors, and $Tu = 3\%$. 43
4.5 Velocity profiles at the diffuser outlet at the time instant $t = 5.5s$, for the three inlet blockage factors, and $Tu = 0.05\%$. . . 44
4.6 Flow uniformity index γ for the three turbulence intensity cases. At every turbulence level, the correspondent simulation with the highest angle at which the flow is attached is marked with a black cross. 45
4.7 C_P (continuous line) and η (dashed line) at different inlet blockage factors (inlet velocity profiles) for Tu = 10%. 46

4.8 C_P (continuous line) and η (dashed line) at different inlet blockage factors (inlet velocity profiles) for Tu = 3%. 47
4.9 C_P (continuous line) and η (dashed line) at different inlet blockage factors (inlet velocity profiles) for Tu = 0.05%. 48
4.10 Modified effectiveness $\bar{\eta}$ for the three turbulence intensity cases. 52
4.11 Blockage factor at the diffuser outlet for the three turbulence intensity cases. 53

5.1 Side view schematic of planar jet wind tunnel. Flow is generated by a centrifugal blower (A), transferred to the pre-settling chamber (B), and then to the rectangular prism section via two tubes (C). Flow passes through the glass spheres (D) where some of the turbulence is killed. After that, honeycomb (E) helps to straighten the flow. Flow is then forced through a set of screens (F) to decrease the turbulence level again. Contraction (G) accelerates the flow before the exit section. [22] . . . 60
5.2 Render of the assembly to be flanged on the planar jet wind tunnel of Figure 5.1 to test the different diffusers. 62
5.3 Cross section of the assembly of Figure 5.2. 62

List of Tables

4.1 Maximum value of C_P, η and $\bar{\eta}$ and their corresponding divergence angle 2θ, for the different turbulence intensity cases. . . 54

List of Symbols

Abbreviations

CFD	Computational Fluid Dynamics
DNS	Direct Numerical Simulations
LES	Large Eddy Simulation
NS	Navier-Stokes
RANS	Reynolds-Averaged Navier-Stokes
SST	Shear Stress Transport
SSTLM	Shear Stress Transport Langry Menter

Notation

α	Velocity profile energy coefficient $= \int_0^{W_1} U^3 dy / \bar{U}^3 A$
$\bar{\eta}$	Modified effectiveness $= C_P / \overline{C_{Pid}}$
$\boldsymbol{u}$	Velocity vector field
δ	Kronecker delta
δ^*	Displacement thickness
η	Effectiveness $= C_P / C_{Pid}$
γ	Intermittency
μ	Dynamic viscosity
ν	Kinematic viscosity
ν_t	Eddy viscosity
ω	Specific energy dissipation rate
$\overline{C_{Pid}}$	Modified ideal static pressure recovery coefficient $= (DF)_1^2 - 1/(AR)^2$
ρ	Density

θ	Half divergence angle of the diffuser
ε	Energy dissipation rate
AR	Area ratio $= A_2/A_1$
AS	Aspect ratio $= b/W_1$
B	Inlet blockage factor $= \frac{2\delta_1^*}{W_1} = B_1$
b	Diffuser span width
B_2	Outlet blockage factor $= \frac{2\delta_2^*}{W_2}$
C_P	Static pressure recovery coefficient $= (\bar{P}_2 - \bar{P}_1)/\bar{q}_1$
C_{Pid}	Ideal static pressure recovery coefficient $= 1 - 1/(AR)^2$
k	Turbulence kinetic energy
N	Diffuser length
q	Dynamic pressure $= \rho\bar{U}^2/2$
Re	Reynolds number $= \bar{U}_1 W_1/\nu$
$Re_{\theta t}$	Transition momentum-thickness Reynolds number
T	Mean natural stall period
t	Characteristic mean time $= N/\bar{U}_1$
W	Diffuser height
DF	Distortion factor $= U_{max}/\bar{U}$

Subscripts

1	Diffuser entrance
2	Diffuser exit
∞	Up-stream component
i, j	i-th and j-th component (Einstein notation)

Abstract

Diffusers are important aerodynamic devices in many engineering applications, but the major part of research in this area is focused on devices operating at high Reynolds numbers. However, in numerous applications, including medical, diffusers may be employed in low Reynolds number flows. A specific feature of this regime is that the flow can undergo a laminar to turbulent transition within the diffuser and this can strongly influence the performance and design of the device. This thesis analyses the effect of inlet conditions on the case of two-dimensional diffusers operating at low Reynolds numbers with a laminar and transitional boundary layer discharging in a stationary atmosphere. Numerical simulations were performed with the joint implementation of the open-source mesh software *Gmsh* and *OpenFOAM*. In particular, 9 different cases are presented varying the inlet turbulence intensity (0.05, 3, and 10 percent) and the inlet velocity profile, characterised by different displacement thicknesses. For each case, a varying number of unsteady CFD simulations were performed using the $k - \omega$ *Transitional SST* RANS model that considers the possible laminarisation of the boundary layer. The pressure recovery coefficient at the outlet is analysed in detail, showing the relevant reduction of pressure recovery in the case of a laminar inlet velocity profile compared with the high Reynolds numbers case in the literature. Furthermore, the use of the modified effectiveness is remarked as an important factor in the analysis of velocity profiles with a high blockage factor. Velocity profiles at the outlet are compared, showing a relevant difference between a

laminar and turbulent velocity profile. Finally, a setup for a future experimental study of two-dimensional diffusers is presented.

Chapter 1

Introduction

Diffusers are devices largely exploited in fluid dynamics applications. They consist of a pipe or channel whose walls diverge in order to increase the cross-sectional area, with the aim of decelerating the main flow while increasing the static pressure at the outlet. The diffuser design is critical because in order to obtain a pressure recovery (difference between inlet and outlet static pressures) a positive pressure gradient must be established, which may lead to separation, hence a detachment of the boundary layer, that is highly dependent on the flow and geometrical conditions. Separation is an extremely relevant phenomenon for aerodynamic performance, although it is extremely difficult to predict due to its non-linear nature.

In diffusers, different regimes can be identified based on the behaviour of the separation point and of the mean flow. If the boundary layer separates, it is said that the diffuser is in a stall regime. These regimes can occur in a large variety of diffuser geometries and flow conditions and they strongly affect the pressure recovery trend. If the diffuser is not well-designed, the static pressure is not recovered due to the high losses and to the blockage effect of the separation bubble which prevents the flow from expanding and causes the flow at the outlet to be non-uniform. Therefore it is important to assess the application in which the diffuser must perform. Typical applications in which large-scale diffusers play an important role are: industrial ventilation, automotive and aeronautics, only to mention some. Diffusers are also important on small-scale devices such as those typical of bio-medical applications (e.g. assisted ventilation pipe systems etc.).

The flow regimes and the diffuser design were extensively studied over the course of the past years. Kline et al. [1] described the optimisation parameters and the relationships between two-dimensional flat, conical and annular diffusers. In 1967 Reneau et al. [2] gathered several two-dimensional diffuser experiments at different divergence angles in order to analyse the pressure recovery and the stall regimes. They concluded that the value of performance is highly affected by inlet conditions and predictions about the location of optimum performance can be made based on correlation, but no analytical model can be used to accurately predict it. Nevertheless, these investigations regard only diffusers operating at high Reynolds numbers and medium-high turbulence levels.

Attention should be given to diffusers operating at low Reynolds numbers, because the flow tends to change regime from turbulent to laminar and the diffuser is prone to separation, presenting a very different behaviour from diffusers operating with a fully turbulent flow. Dighe [3] experimentally tested planar diffusers at low and medium Reynolds numbers but did not test the effect of other relevant inlet conditions, such as inlet velocity profiles and turbulence level, in the presence of low Reynolds numbers. Overall, laminar flow in diffusers is not extensively studied, but it is present in all those applications characterised by small sizes or low velocities, such as medical devices and pipe systems.

1.1 Aim of the thesis

The work of this thesis involves the case of diffusers operating at low Reynolds numbers, as part of a larger work that deals with a study of a non-invasive ventilation (NIV) helmet as support for long periods of treatment of respiratory diseases. This device presents a diffuser to introduce oxygen inside the helmet that must be optimised to increase performance. Nevertheless, there are several difficulties, because the internal flow of these biomedical devices is characterised by strong pressure gradients and small Reynolds numbers due to the small geometries involved, which give rise to a possible laminarisation of the flow.

For this reason, through numerical simulations, this thesis aims to study the behaviour of diffusers at low Reynolds numbers with a range of inlet conditions that can be easily found in biomedical applications of this type. The analysis is focused on two-dimensional diffusers to examine the effect of inlet and boundary conditions more than geometry. Since the existing literature presents correlations between several diffuser geometries, the work of this thesis (focused on two-dimensional diffusers) can be hopefully adapted to various three-dimensional geometries. In any case, this should be verified because the literature correlations focus only on high Reynolds numbers. Besides the low Reynolds number, the inlet conditions taken into account are the turbulence intensity and the velocity profile at the diffuser inlet. To have direct control over inlet conditions, before the diffuser throat, there is only a very short channel of length equal to the inlet width. At the outlet there is no channel, but the diffuser discharges directly in a stationary atmosphere. This complicates the simulations since the flow tends to be very unsteady, therefore steady solutions are not attainable. In addition, the size of the outlet chamber is fundamental, hence a detailed analysis is presented on this aspect. The mesh is created using the open-source software *Gmsh* through the programming language *Python*. Simulations are performed using *OpenFOAM*.

The thesis objectives can be summarised as follows:

- Validation of the CFD model with the high Reynolds numbers data experimentally obtained, described by Reneau et al. [2].

- Analysis of the outlet velocity profiles and comparison of the stall regimes with the high Reynolds numbers case present in literature [2].
- Analysis and comparison of the pressure recovery coefficients and effectiveness curves for the different turbulence intensity cases.

1.2 Thesis outline

The thesis first describes the theoretical background in Chapter 2, initially focusing on diffusers, their stall regimes and the factors that influence pressure recovery most. A literature review concerning the governing equations and the most famous RANS models follows, detailing the one employed in this work.

The geometric configuration, the mesh independence study and the CFD model implementation follow with Chapter 3.

Chapter 4 involves an analysis of the results obtained from the simulations.

Finally Chapter 5 concerns the conclusions about the important aspects that the simulations have revealed. The thesis ends with the design of an experimental setup that can be eventually used to validate the CFD model and obtain new and important results from real diffusers.

Chapter 2

Theoretical background

2.1 Diffusers

The term *diffuser* is used to describe a device whose primary purpose is to convert the kinetic energy of the flow (dynamic pressure) into static pressure, lowering the stream velocity and limiting the pressure losses. There are different possible shapes but the common characteristic is an increment of cross-sectional area by means of diverging walls such that a positive (adverse) pressure gradient is established. The typical diffuser shapes are conical, pyramidal and planar, named based on the shape of the cross-section and the diverging walls. Some examples are shown in Figure 2.1.

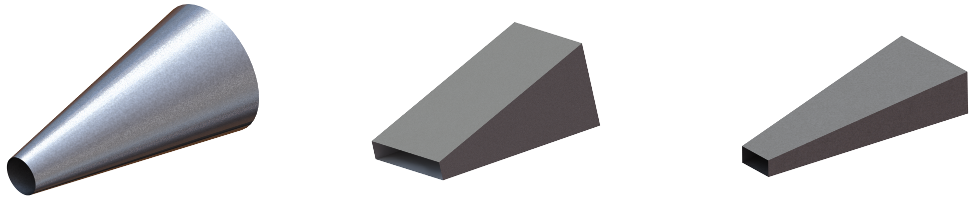

(a) Conical diffuser (b) Planar diffuser (c) Pyramidal diffuser

Figure 2.1: Examples of the canonical diffuser shapes. Planar diffusers can be considered two-dimensional if the inlet has a large aspect ratio $AS > 1$.

For the continuity equation, the mean flow must slow down if an increment of cross-sectional area is present, and a lower normal velocity is expected to respect mass conservation (if the flow is subsonic). The difficulty in designing a diverging wall is that the boundary layer is inclined to separate because of the adverse pressure gradient. These separations are highly dependent on the free stream conditions as well as geometry. Increasing the pressure gradient brings a higher pressure recovery as well as an increased chance of separation.

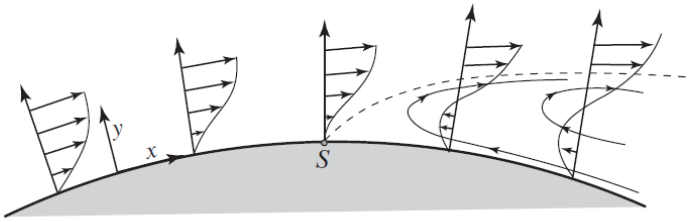

Figure 2.2: Sketch of boundary layer separation (G. Buresti [4], 2012, p.214).

The separation point (S in Figure 2.2) is defined as the point where the wall viscous shear stress is zero and $\partial u/\partial y = 0$ at the wall. A necessary condition for boundary layer separation is an adverse pressure gradient ($dp/dx > 0$) which verifies in diffusers due to diverging walls. This condition is not sufficient for separation: in fact, if the pressure gradient is not strong enough, the boundary layer does not detach from the wall. This condition can be obtained for short diverging walls and small angles.

Predicting the separation point is not easy because the phenomenon is highly unsteady and the hypothesis concerning a thin boundary layer cannot be used for analytical analysis. In particular, it is no longer true that $\partial u/\partial x << \partial u/\partial y$ close to the surface; in addition, the normal velocity component v cannot be assumed to be of a small order of magnitude compared to tangential component u [4].

In some cases, the boundary layer can experience reattachment to the wall after separation. Specifically, this can happen in case of geometry-induced separation (e.g. sharp corners, rarely present in diffusers) or in case of turbulent transition after a laminar transition thanks to a redistribution of high-momentum flow near the wall due to turbulence. Indeed, when the boundary layer is laminar, it tends to separate more easily due to low momentum close to the wall. Once it is separated it can create a recirculation bubble and it quickly becomes turbulent. In general aerodynamic applications, boundary layer separation tends to be avoided; however, for diffusers, it could be useful to reach the edge of the early stage of stall, namely a regime that consists in unsteady detachments and following reattachments of the boundary layer, where the peak of pressure recovery can be found.

There exist methods to energise the boundary layer and to control the separation, by means of both active and passive control. For example, wall suction, blowing and vortex generators can be exploited. In the present work, no separation control devices are considered.

Many parameters can be used in characterising and optimising the performance of diffusers, mostly based on the application. The *static pressure recovery coefficient* C_P is the most used one. It is defined as:

$$C_P = \frac{\bar{P}_2 - \bar{P}_1}{\bar{q}_1} \tag{2.1}$$

where $\bar{P}_2$ and $\bar{P}_1$ are respectively the static pressures at the outlet and inlet of the diffuser, while $\bar{q}_1$ represents the dynamic pressure of a uniform flow at the inlet. It is important to maximise the pressure recovery coefficient because this would mean minimising the losses and maximising the potential pressure obtainable from the increase of cross-sectional area. In fact, static pressure is not recovered if the effective cross-sectional area is reduced due to separation bubbles. Another relevant parameter is the effectiveness η, defined as:

$$\eta = \frac{C_P}{C_{Pid}} \tag{2.2}$$

where $C_{Pid} = 1 - 1/A_R^2$, AR is the area ratio A_2/A_1. C_{Pid} is the pressure recovery coefficient that can be obtained assuming that the flow expands with no losses and the velocity profile is uniform across each section. It can be obtained from the Bernoulli and continuity equations:

$$\begin{cases} \bar{P}_1 + \bar{q}_1 = \bar{P}_2 + \bar{q}_2 \\ A_1\bar{U}_1 = A_2\bar{U}_2 \end{cases} \tag{2.3}$$

In some applications it could be necessary to have a uniform outflow minimising oscillations, which is why a uniformity coefficient could be considered. The flow uniformity index proposed by Daniels et al. [5] can be exploited:

$$\gamma = 1 - \frac{1}{W_2}\int_y \frac{\Phi}{2U_{ave}}dy \qquad \text{where } \Phi = ||U| - U_{ave}|, \qquad U_{ave} = \frac{1}{W_2}\int_y |U|dy \tag{2.4}$$

where W_2 is the diffuser width at the outlet. In the description and correlations of diffuser performance, it can be useful to define some geometrical coefficients that refer to the geometry of Figure 2.3. The area ratio $AR = A_2/A_1$ is linked to the divergence angle θ in the case of straight-walled diffusers. The diffuser length N, defined as the distance between the throat and the outlet can be adimensionalised with the throat (inlet) width W_1 to create the coefficient N/W_1. The length L of the diverging walls is not usually exploited. In the case of real three-dimensional diffusers, it is important to consider the aspect ratio, defined as $AS = b/W_1$, where b is the span width.

An important flow parameter is the blockage factor B that was found to easily correlate the different inlet velocity profile effects. This is the adimensional displacement thickness defined as follows:

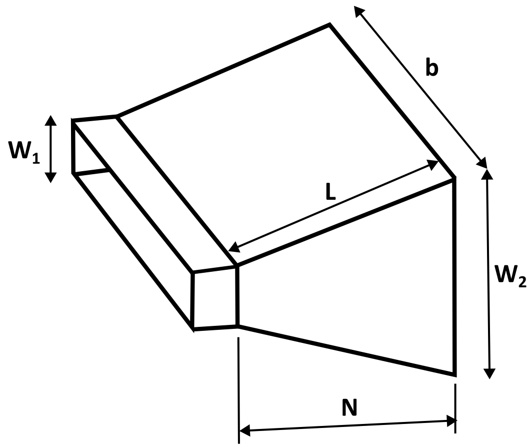

Figure 2.3: Geometry of three-dimensional straight-walled diffusers.

$$B = \frac{2\delta_1^*}{W_1} = \frac{1}{W_1}\int_0^{W_1}\left(1 - \frac{U}{U_{max}}\right)dy = 1 - \frac{\bar{U}}{U_{max}} \tag{2.5}$$

where δ^* is the displacement thickness.

The blockage factor represents the obstruction of the flow due to the boundary layer; therefore, the effective area fraction available for the expansion of the flow is lower. This largely impacts on the diffuser performance. Figure 2.4 shows the displacement thickness of a velocity profile in an internal flow.

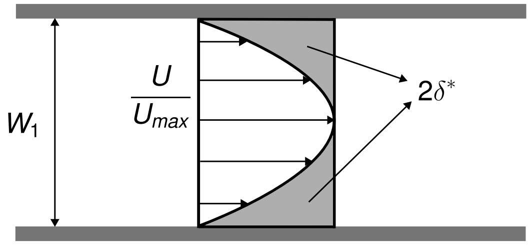

Figure 2.4: Representation of the displacement thickness in an internal flow.

Increasing the divergence angle of the diffuser, the adverse pressure gradient increases as well as the chance of boundary layer separation and eventual flow reattachment regions. Kline et al. [1] and Reneau et al. [2] described the stall patterns by flow visualisation and created the charts of Figure 2.5 that link the flow regime to the diverging angle and diffuser length. The different flow regimes that can be established, affect the pressure recovery in a relevant way. The classical stall pattern that can be observed in external flow does not always accurately describe stall in diffusing passages. The latter can be described by four patterns.

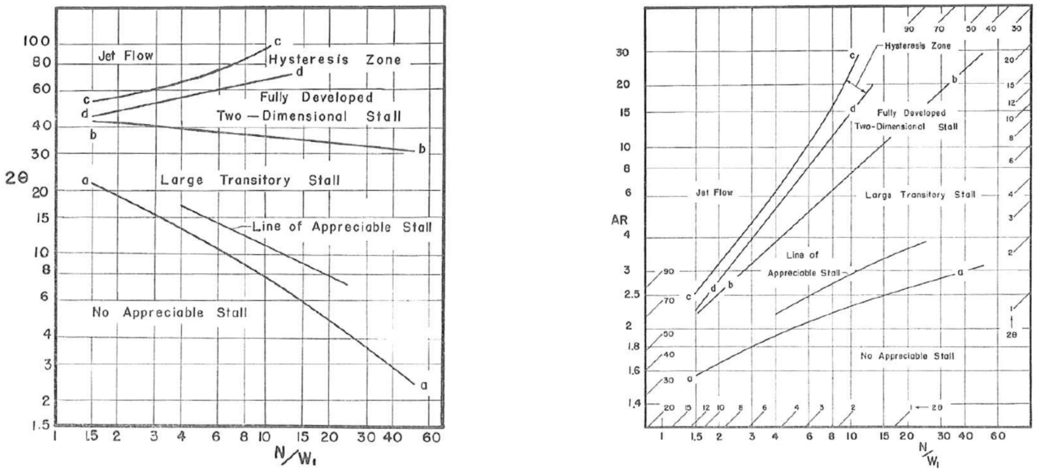

(a) 2θ - N/W_1 plane

(b) AR - N/W_1 plane

Figure 2.5: Flow regimes in straight-wall, 2D diffusers, $Re > 10^4$ [2].

No appreciable stall regime

This pattern is present only for small angles and area ratios (A_2/A_1) where there is no appreciable stall visible, at most only in some parts. This corresponds to the area limited by line a-a in figure 2.5. The pressure and velocity profiles are symmetrical about the centre plane.

Large transitory stall regime

During this pattern many fluctuations are observed, with stalled regions that constantly form in and are subsequently washed out of the diffuser, causing large pressure fluctuations as a consequence. The position of the transient stall varies with the geometry of the diffuser but in general, in wide diffusers ($N/W_1 < 4$), the transitory stall occurs in one diverging wall, hence the flow remains fixed near one diverging wall and the stalls build up and are washed out on the other diverging wall. In narrow diffusers ($N/W_1 > 16$), the stall occurs on both parallel walls. In the latter case, a blockage effect is visible, which holds away the thorough flow. The region lies between curves a-a and b-b in Figure 2.5.

Two-dimensional flow regime

This pattern represents a steady, two-dimensional stall, where the flow separates near the throat and follows one diverging wall. Performances are low due to the large blockage effect, therefore the separated region acts as an obstruction to the incoming flow. If an important disturbance is present, the stall could be switched from one diverging wall to the other. This region lies above line b-b in figure 2.5.

Jet flow regime

In this pattern, a jet flow is present because the incoming flow separates from both diverging walls very near the throat and proceeds straight down the diffuser. Velocity and pressure are relatively steady, compared to the previous stall regimes. This region lies above line c-c but it can exist down to line d-d in figure 2.5.

Figure 2.6 represents the pressure recovering, varying the area ratio or the angle, as well as the correspondent flow regimes. It is observed that the best pressure recovery verifies just after line a-a, therefore after the large transitory stall, when both side walls present an unsteady reverse flow. Nonetheless, the aperture angle should not cause the two-dimensional stall, otherwise a consistent pressure loss occurs [7].

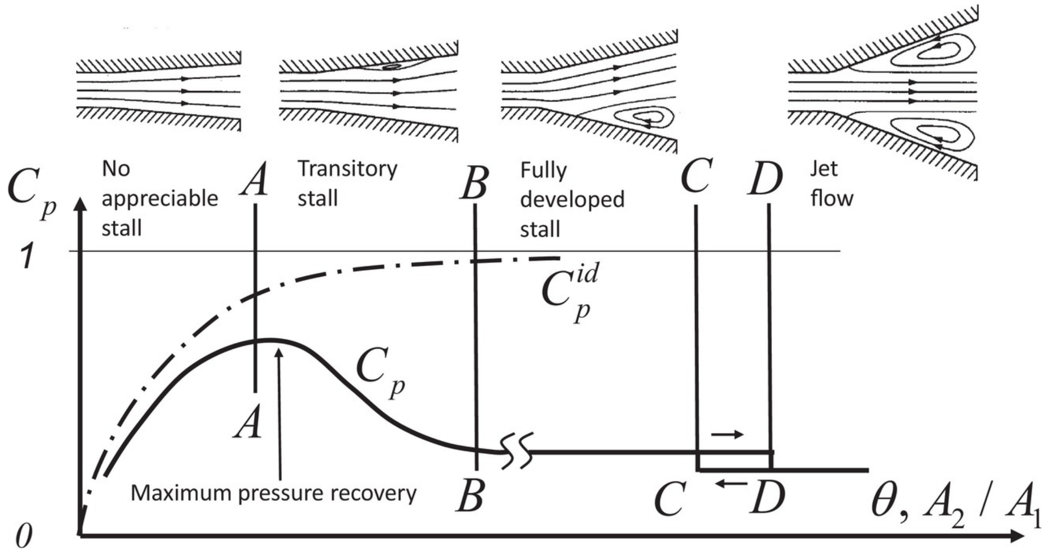

Figure 2.6: Relationship between flow regime and pressure recovery coefficient (Casey and Robinson [6], 2021, p.231).

2.1.1 *Influence of inlet and outlet conditions*

The angles at which stall occurs and, more in general, the diffuser performance, are strongly influenced by flow conditions at the inlet. There are parameters that influence performance more than others and only in determined conditions. The inlet conditions to be considered are the turbulence level, the flow swirl, the boundary layer thickness (blockage factor), the shape of the velocity profile, the inlet Reynolds number and the Mach number.

All the previous considerations about stall regimes refer to a fully turbulent and thin boundary layer at the throat, corresponding nearly to a top-hat velocity profile. With a high Reynolds number ($Re > 10^4$) it was found that the Reynolds number itself does not seem to have an important effect [2] [3]. This is not true if the Reynolds number is low enough ($Re < 10^3$) to maintain the inlet boundary layer laminar or transitional, because, as explained earlier, a laminar boundary layer has a lower momentum, therefore it is more likely to separate at the throat. Another relevant effect of the

Reynolds number is that it determines the boundary layer thickness at the throat, while a negligible effect is the rate of growth of the boundary layer within the diffuser [8].

Dighe [3] experimentally analysed plane diffusers changing the Reynolds numbers and the aspect ratio. A monotonic increase in pressure recovery was found increasing the Reynolds number from laminar to turbulent flow (from 2500 to 20000). Above 20000 the pressure recovery remained constant. When $Re < 5000$, the Reynolds number became a controlling flow regime parameter. Nevertheless, most literature focused on diffusers operating at high Reynolds numbers, mainly because they cover the majority of industrial applications.

In the case of a fully turbulent inlet velocity profile, inlet flow with a turbulence intensity of less than about 3 percent will not affect the flow pattern, while for higher turbulent flows (10 percent), line b-b could be higher (figure 2.5).

Another conclusion concerning the boundary layer is that displacement thickness takes an important role in determining both the flow pattern and the pressure recovery, in fact, a small change in displacement thickness could change pressure recovery up to 10-20 percent [2]. The throat aspect ratio AS has little or no effect on the flow regime as long as $AS > 1$ [2].

The characteristic mean time for a fluid particle to pass through the diffuser is given by the ratio of diffuser length to the inlet velocity, $t = N/\bar{U}_1$. In all regimes, the flow variations have a period of order $10t$. Differently, in the transitory stall regime, the pressure and large flow variations require a mean time of order $100t$ to complete a cycle [2].

Since the transitory stall flow regime is unsteady but it presents a certain degree of periodicity, Smith et al. [9] characterised the mean times and distribution of stall build-up and wash-out periods. Defined the mean natural stall period (T_N) as large sample time averages evaluated from flow visualization of consecutively occurring stall periods, it is possible to characterise the stall. Stall wash out periods are quasi-periodic with a standard deviation of $\sigma \approx \pm 0.5\, \bar{T_N}$. In the transitory stall regimes, outflow unsteadiness increases rapidly with increased included angle, indeed it is observed at approximately $2\theta = 20° \ to \ 24°$. It is important to underline the fact that Smith et al. [9] analysed diffusers at a high Reynolds number, therefore previous conclusions could be different for diffusers operating at $Re < 10^4$.

Kwong and Dowling [10] analysed the unsteadiness of the stalled flow, following the work of Smith Jr and Kline [9]. They found that the duct to which the diffuser is connected has an important relevance on the stall frequency. Furthermore, they found that the maximum fluctuations frequency is observed in the middle of the transitory stall regime, as shown by Smith Jr and Kline [9] as well.

Diffusers deal with internal flows, but at the outlet the situation can vary depending on the application in which the diffuser is involved. In fact, it is possible to have either a tailpipe or a plenum exit condition. A tailpipe is a duct at the end of diverging walls, that lets the flow even out and brings higher pressure recovery due to confinement. Conversely, a plenum exit condition means that the diffuser discharges directly in a stationary atmosphere, which induces higher unsteadyness. This has a strong repercussion on numerical simulations because steady CFD solvers cannot be used. Indeed, the solution would oscillate and never converge to a certain field value. Unsteady CFD simulations have to be used instead, which complicates the analysis because the simulation time becomes an important parameter that is not always known a priori.

2.2 Governing equations and turbulence modelling

2.2.1 Governing equations and DNS

The so-called Navier-Stokes (NS) equations are a mathematical model based on fluid assumptions formulated more than a century ago and recognised as the most accurate model describing the behaviour of single-phase flows. The important drawback of these equations is that it is not known if there exists an analytical solution and whatever it may be. Since the present thesis deals with incompressible and subsonic flows, the governing equations can be considered to be only mass conservation (Equation 2.6) and momentum conservation (Equation 2.7); therefore the energy equation is not considered. In addition, density ρ could be considered constant, which makes the velocity field solenoidal. Nevertheless, in the following equations, density will be considered to be a non-constant scalar field for completeness.

$$\frac{\partial \rho}{\partial t} + \frac{\partial}{\partial x_j}\left[\rho u_j\right] = 0 \tag{2.6}$$

$$\frac{\partial}{\partial t}\left(\rho u_i\right) + \frac{\partial}{\partial x_j}\left[\rho u_i u_j + p\delta_{ij} - \tau_{ji}\right] = 0, \quad i = 1, 2, 3 \tag{2.7}$$

where:
u is the Velocity vector field
δ is the Kronecker delta
τ_{ij} is the shear stress tensor

Since the previous equations do not have an analytical solution for a general case, a numerical way to solve them has been considered for over 60 years. The range of techniques that have been employed in the numerical solution of these equations form the field known as Computational Fluid

Dynamics (CFD).

Turbulence has a decisive influence on most applications; dealing with diffusers means having strong separations and reattachments that are governed mostly by turbulence. Turbulent flows are characterised by velocity fluctuations and eddies. In order to numerically solve them in an adequate manner, it is necessary to use a very fine mesh, finer than the smallest length scale and a time step smaller than the fastest fluctuation of the flow. The range of these scales is dependent on the Reynolds number. This means that if a flow presents a high Reynolds number it will be characterised by a wide range of temporal and spatial scales. The computational cost is proportional to these scales. In particular, the computational cost scales with $Re^{3.3}$ for wall-bounded flows if Navier-Stokes equations are solved without any simplifications; this method is called DNS, Direct Numerical Simulations. Therefore, solving a common industrial application would require years for a supercomputer. Nowadays, DNS simulations are only performed for academic purposes and for canonical flow fields and geometries, like pipe and channel flows, in order to take them as benchmarks.

Methods to reduce the computational cost of such simulations employ simplifications; the exact NS equations can be time-averaged, ensemble-averaged or manipulated to remove the smallest scales. At the same time, this means introducing a certain error, whose degree depends on the application and on coefficients used to tune these new models.

To reduce the computational cost, the effect of turbulence is modelled. In general, the amount of this modelled turbulence is proportional to the saved time. The most famous models are RANS (Reynolds-Averaged Navier-Stokes) and LES (Large Eddy Simulation). RANS modelling is explained in the following paragraph because it is the simplification embedded in the model used for the simulations performed for this thesis.

2.2.2 RANS

RANS models are the most applied in industrial applications thanks to the reduced computational cost which allows to simulate complex geometries with sufficient accuracy.

They are based on Reynolds decomposition, whereby a fluctuating field can be expressed as the sum of its average and its fluctuating part (Equation 2.8). Once the new velocity field expressed in the Reynolds decomposition is included in the NS equations 2.6 and 2.7, and equations are averaged, RANS equations are obtained (2.9 and 2.10) [11]. These equations represent the motion of the average flow, taking into account the fluctuations due to turbulence expressed by the Reynolds stress ($-\rho\overline{u_i'u_j'}$), acting as a stress term; therefore RANS equations aim to model this term.

$$u_i(\boldsymbol{x},t) = \bar{u}_i(\boldsymbol{x}) + u_i'(\boldsymbol{x},t) \tag{2.8}$$

$$\frac{\partial \bar{u}_i}{\partial x_i} = 0 \tag{2.9}$$

$$\rho \bar{u}_j \frac{\partial \bar{u}_i}{\partial x_j} = \rho \bar{f}_i + \frac{\partial}{\partial x_j}\left[-\bar{p}\delta_{ij} + \mu\left(\frac{\partial \bar{u}_i}{\partial x_j} + \frac{\partial \bar{u}_j}{\partial x_i}\right) - \rho\overline{u_i'u_j'}\right] \tag{2.10}$$

The Reynolds stress can be modelled in different ways, here it is explained the one used for the present work. One of them relies on the Boussinesq hypothesis. It is based on the concept that turbulent mixing acts in a similar way as molecular mixing, proposed by Boussinesq in 1877 for the mixing thin shear layers [12]. In addition, it consists on the alignment of the Reynolds stress tensor with the strain tensor of the mean flow.

$$-\overline{u_i'u_j'} = \nu_t\left(\frac{\partial \overline{u_i}}{\partial x_j} + \frac{\partial \overline{u_j}}{\partial x_i}\right) - \frac{2}{3}k\delta_{ij} \tag{2.11}$$

where:
ν_t is the turbulence eddy viscosity

$k = \frac{1}{2}\overline{u_i' u_i'}$ is the turbulence kinetic energy

The eddy viscosity cannot be assumed to be constant but rather governed by the length scale (Λ) and velocity scale (V) of the large energetic eddies.

$$\nu_t \sim \Lambda V \tag{2.12}$$

Therefore, the solution of the RANS equations is now based on the modelling of the eddy viscosity, or equivalent, the modelling of the length and velocity scales.

There exist different ways to model eddy viscosity:

- **Algebraic models, or zero equation models**: Length and velocity scales are modelled based on the characteristic mean flow velocity and geometry. This way of modelling the eddy viscosity gives accurate results just for thin and attached boundary layers, therefore it is not general.
- **One-equation models**: one equation is solved, usually a transport equation for the turbulence kinetic energy k or the eddy viscosity. These models are good for attached and thin boundary layers.
- **Two-equation models**: Two transport equations are solved for two different variables, for example, turbulence kinetic energy k and specific energy dissipation rate ε. These models are considered complete because no other quantities are needed for the solution of such models. Nevertheless, they can be improved by the solution of other quantities like the distance from the wall. They perform better than the previous models and certain two-equation models are suitable for separation and detached boundary layers.

Among the two-equation models, the most common are the $k-\varepsilon$ model and the $k-\omega$ model with its variant $k-\omega\ SST$. Now a brief introduction of these two models is made, focusing on the model used for this work, the $k-\omega\ Transitional\ SST$ model.

$k - \varepsilon$ model

The $k - \varepsilon$ model [13] is one of the most used CFD models because it gives accurate results with a relatively low computational cost. It is a two-equation model based on turbulence kinetic energy k and its dissipation rate ε. They have to be solved together with the RANS equations for the mean flow. The model is complete because the eddy viscosity ν_t (2.12) is derived from the two transport equations k and ε.

$$\nu_t = C_\mu \frac{k^2}{\varepsilon} \tag{2.13}$$

where C_μ is a model coefficient, usually $C_\mu = 0.09$.

It is assumed that the kinetic energy dissipation rate at small scales is in equilibrium with energy transfer rate from largest scale. This is the hypothesis in order to write the eddy viscosity as function of ε.

$$\frac{\partial(\rho k)}{\partial t} + \frac{\partial(\rho k \bar{u}_i)}{\partial x_i} = \rho P + \frac{\partial}{\partial x_j}\left[\left(\mu + \frac{\mu_t}{\sigma_k}\right)\frac{\partial k}{\partial x_j}\right] - \rho\varepsilon \tag{2.14}$$

$$\frac{\partial(\rho \varepsilon)}{\partial t} + \frac{\partial(\rho \varepsilon \bar{u}_i)}{\partial x_i} = \frac{\partial}{\partial x_j}\left[\left(\mu + \frac{\mu_t}{\sigma_\varepsilon}\right)\frac{\partial \varepsilon}{\partial x_j}\right] + C_{1\varepsilon}\frac{\varepsilon}{k}\rho P - C_{2\varepsilon}\rho\frac{\varepsilon^2}{k} \tag{2.15}$$

where:

$$P = \tau_{ij}\frac{\partial \bar{u}_i}{\partial x_j}$$

$\mu_t = \rho\nu_t$

$C_{1\varepsilon} = 1.44, \quad C_{2\varepsilon} = 1.92, \quad \sigma_k = 1.0, \quad \sigma_\varepsilon = 1.3$

The different model coefficients are calibrated for some generic cases where some of the terms vanish. These cases include decaying isotropic and homogeneous turbulence, homogeneous shear flow and the log layer in the boundary layer.

This model is indicated when the flow is turbulent, low pressure gradients are present and where the Reynolds shear stresses are most important. However, this model performs poorly where large pressure gradients are present and in unconfined flows.

The $k - \varepsilon$ model requires wall functions in order to model the boundary layer because the last term of equation 2.15 (destruction term) would tend to infinity close to the wall, as k goes to zero at the wall. For this reason typically $y^+ > 30$.

$\boldsymbol{k - \omega}$ model

The $k - \omega$ model [14] is another two-equation model that is widely used. It considers ω (frequency of the large eddies or specific energy dissipation rate) instead of ε. Usually, ω is defined as:

$$\omega \equiv \frac{\varepsilon}{C_\mu k} \tag{2.16}$$

The eddy viscosity is now defined as:

$$\nu_t = \frac{k}{\omega} \tag{2.17}$$

Therefore the two transport equations are those for k and ω:

$$\frac{\partial(\rho k)}{\partial t} + \frac{\partial(\rho \bar{u}_j k)}{\partial x_j} = \rho P - \beta^* \rho \omega k + \frac{\partial}{\partial x_j}\left[\left(\mu + \sigma_k \frac{\rho k}{\omega}\right)\frac{\partial k}{\partial x_j}\right] \tag{2.18}$$

$$\frac{\partial(\rho \omega)}{\partial t} + \frac{\partial(\rho \bar{u}_j \omega)}{\partial x_j} = \frac{\alpha \omega}{k}\rho P - \beta \rho \omega^2 + \frac{\partial}{\partial x_j}\left[\left(\mu + \sigma_\omega \frac{\rho k}{\omega}\right)\frac{\partial \omega}{\partial x_j}\right] \tag{2.19}$$

where:

$$P = \tau_{ij}\frac{\partial \bar{u}_i}{\partial x_j}$$

$\alpha = 5/9, \quad \beta = 3/40, \quad \beta^* = 9/100, \quad \sigma_k = 1/2, \quad \sigma_\omega = 1/2$

Unlike the $k-\varepsilon$ model, here there is not any singularity at the wall related to the ratio $1/k$, present in the destruction term of ε instead. However, a problem is related to the turbulence variable ω because it tends to infinity at the wall ($\sim \varepsilon/k$). This can be overcome by applying a high value of ω at the wall. The turbulence quantities are not asymptotically accurate close to the wall, but the mean flow is reasonably well predicted. The major problem with the $k-\omega$ model is the strong free-stream turbulence level sensitivity, supposed to be caused by the turbulence interfaces (e.g. boundary layer interface).

Nevertheless, this model can more accurately predict flows that present high pressure gradients, unlike the $k-\varepsilon$ model.

Furthermore, unlike the $k-\varepsilon$ model, here the boundary layer can be completely resolved up to the wall ($y^+ \approx 1$) for better accuracy.

$k-\omega$ *SST* model

The Shear Stress Transport (SST) model [15] is a modification of the standard $k-\omega$ model in order to avoid the strong dependency on the free-stream turbulence level. This model combines the $k-\varepsilon$ model out of the boundary layer and the $k-\omega$ model close to the wall. The two transport equations are the k equation and the ω equation, the latter reformulated as follow:

$$\begin{aligned}\frac{\partial(\rho\omega)}{\partial t} + \frac{\partial(\rho\bar{u}_j\omega)}{\partial x_j} = \frac{\alpha\omega}{k}\rho P - \beta\rho\omega^2 + \frac{\partial}{\partial x_j}\left[\left(\mu + \sigma_\omega\frac{\rho k}{\omega}\right)\frac{\partial\omega}{\partial x_j}\right] \\ + 2(1-F_1)\frac{\rho\sigma_{\omega2}}{\omega}\frac{\partial k}{\partial x_j}\frac{\partial\omega}{\partial x_j}\end{aligned} \tag{2.20}$$

$\alpha = 5/9, \quad \beta = 3/40, \quad \beta^* = 9/100, \quad \sigma_\omega = 1/2, \quad \sigma_{\omega2} = 0.856$
F_1 is a blending function

The blending function F_1 gives a smooth transition between $k-\varepsilon$ far from the wall and $k-\omega$ close to the wall, exploiting the distance of the mesh cell from the closest wall. F_1 goes from 0 to 1. It is 1 when the last term (cross-diffusion) must be null and therefore in correspondence with the $k-\omega$ model (Equation 2.19). It is 0 when the model must correspond to $k-\varepsilon$ instead. In fact, considering the definition of ω given by Equation 2.16 and substituting it in Equation 2.15, the last term of Equation 2.20 appears.

Another feature of the $k-\omega$ SST model is the viscosity limiter that gives better results in agreement with experimental data of separated flows. In fact, there is an over-prediction of the wall shear stress if a limiter is not exploited. Therefore the $k-\omega$ SST model can more accurately predict separation compared to the previous models explained. The boundary conditions are the same as the $k-\omega$ model. As the standard $k-\omega$ model, the boundary layer can be completely resolved down to the wall ($y^+ \approx 1$).

$k-\omega$ *Transitional SST* ($SSTLM$) model

The $k-\omega$ $Transitional\ SST$ (or $SSTLM$ from the researchers Langry and Menter that developed this model) [16] [17] is a modification of the standard $k-\omega$ SST model (Equations 2.18 and 2.20) that includes two additional transport equation: γ and $\hat{Re}_{\theta t}$.

The main objective of this model is to maintain the positive proprieties of the $k-\omega$ SST model, in particular the ability to predict the separation accurately, while offering the possibility to simulate flows at low Reynolds numbers, therefore presenting transition regions or laminar regions.

$$\begin{aligned} \frac{\partial(\rho k)}{\partial t} + \frac{\partial(\rho \bar{u}_j k)}{\partial x_j} &= \gamma \rho P - \beta^* \rho \omega k * min(max(\gamma, 0.1), 1) \\ &+ \frac{\partial}{\partial x_j}\left[\left(\mu + \sigma_k \frac{\rho k}{\omega}\right)\frac{\partial k}{\partial x_j}\right] \end{aligned} \tag{2.21}$$

$$\begin{aligned} \frac{\partial(\rho \omega)}{\partial t} + \frac{\partial(\rho \bar{u}_j \omega)}{\partial x_j} = \frac{\alpha \omega}{k}\rho P - \beta \rho \omega^2 + \frac{\partial}{\partial x_j}\left[\left(\mu + \sigma_\omega \frac{\rho k}{\omega}\right)\frac{\partial \omega}{\partial x_j}\right] \\ + 2(1-F_1)\frac{\rho \sigma_{\omega 2}}{\omega}\frac{\partial k}{\partial x_j}\frac{\partial \omega}{\partial x_j} \end{aligned} \tag{2.22}$$

$$\frac{\partial(\rho\gamma)}{\partial t}+\frac{\partial(\rho u_j\gamma)}{\partial x_j}=P_\gamma-E_\gamma+\frac{\partial}{\partial x_j}\left[\left(\mu+\frac{\mu_t}{\sigma_f}\right)\frac{\partial\gamma}{\partial x_j}\right] \tag{2.23}$$

$$\frac{\partial\left(\rho\hat{R}e_{\theta t}\right)}{\partial t}+\frac{\partial\left(\rho u_j\hat{R}e_{\theta t}\right)}{\partial x_j}=P_{\theta t}+\frac{\partial}{\partial x_j}\left[\sigma_{\theta t}\left(\mu+\mu_t\right)\frac{\partial\hat{R}e_{\theta t}}{\partial x_j}\right] \tag{2.24}$$

where:
$\alpha = 5/9, \quad \beta = 3/40, \quad \beta^* = 9/100, \quad \sigma_k = 1/2$
$\sigma_\omega = 1/2, \quad \sigma_{\omega 2} = 0.856, \quad \sigma_f = 1.0, \quad \sigma_{\theta_t} = 2.0$
F_1 is a blending function
P_γ is the production term of the γ transport equation
E_γ is the dissipation term of the γ transport equation
$P_{\theta t}$ is the production term of the $Re_{\theta t}$ transport equation

The Transport variable γ is called *Intermittency* and it represents the percentage of time that fluctuations are locally present in the boundary layer: if it is 0 it means the flow is locally laminar, while if it is 1 it means the flow is locally fully turbulent. It can be noticed that γ is present in equation 2.21, acting on the production and dissipation terms. Concerning the production term, this is modified in the case of laminar flow because no production of kinetic energy is present. At the same time, since the boundary layer is laminar, the dissipation must be reduced.

The transport equation for the variable ω assumes the same form as Equation 2.20, but the blending function F_1 is modified to avoid the switching to $k-\varepsilon$ in case of laminar boundary layer.

Equation 2.23 is the transport equation for the intermittency variable γ and it assumes the same form as the other transport equations, therefore there is a production, dissipation and transport term with the proper tuning coefficients. Where the flow is laminar, P_γ is expected to be 0 while in transition regions P_γ saturates to 1. The dissipation term E_γ allows the flow to re-laminarise in case there were the necessary flow conditions.

The production term depends on additional functions that determine when the production term itself has to be switched on and how quickly,

therefore controlling the length of the transition region. These functions depend on two main variables, $Re_{\theta c}$ and $Re_{\theta t}$. They respectively represent the momentum-thickness Reynolds number at which fluctuations start increasing and at which transition begins. $Re_{\theta c}$ is always smaller than $Re_{\theta t}$. Both $Re_{\theta c}$ and $Re_{\theta t}$ are function of the transport variable $\hat{Re}_{\theta t}$ solved by the Equation 2.24.
$P_\gamma = f(Re_{\theta c}, Re_{\theta t}) \quad Re_{\theta c} = f(\hat{Re}_{\theta t}) \quad Re_{\theta t} = f(\hat{Re}_{\theta t})$

The $\hat{Re}_{\theta t}$ is solved by Equation 2.24, which presents a production term $P_{\theta t}$ that forces the variable to its free-stream value based on the boundary conditions. Then it is diffused towards the wall, where it takes the local value that is finally used to determine the local production term for the intermittency variable.

To close the model, an empirical correlation is required. Usually the free-stream value of $Re_{\theta t}$ is defined as:

$$\hat{Re}_{\theta t} = \begin{cases} 1173.51 - 589.428Tu + \frac{0.2196}{Tu^2} & \text{if } Tu \leq 1.3 \\ \frac{331.5}{(Tu-0.5658)^{0.671}} & \text{if } Tu > 1.3 \end{cases} \tag{2.25}$$

where:

$$Tu = 100\frac{\sqrt{2/3k}}{|\boldsymbol{u}_\infty|} \tag{2.26}$$

Concerning the other boundary conditions, at the inlet $\gamma = 1$, while at the wall $\frac{\partial}{\partial n}\gamma = 0$ and $\frac{\partial}{\partial n}\hat{Re}_{\theta t} = 0$.

Overall, this model can provide very good accuracy if the flow presents some laminar or transitional regions, therefore suitable in cases in which the Reynolds number is sufficiently low. Nevertheless, a careful choice of inlet/free-stream value of $Re_{\theta t}$ is fundamental, as well as having a mesh that is resolved down to $y^+ < 1$. Since the model has four partial differential equations to be solved, the computational cost slightly increases.

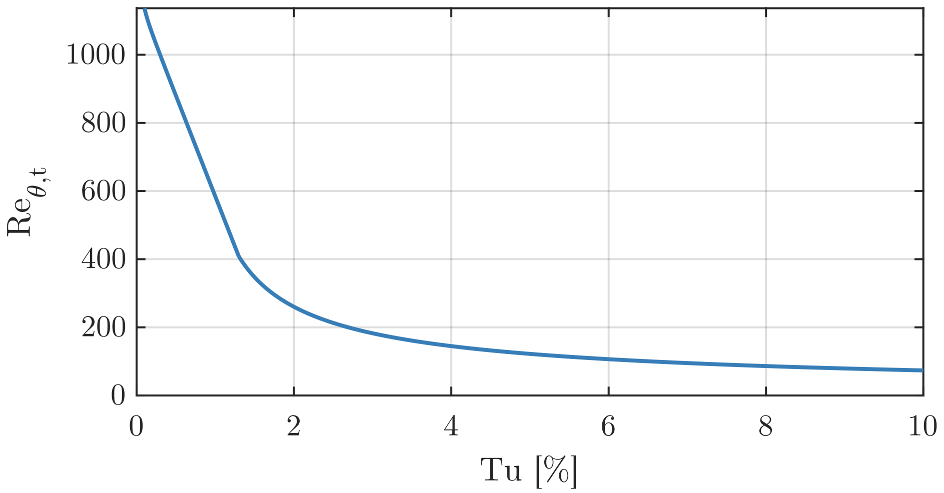

Figure 2.7: Empirical relationship given by Equation 2.25 which defines the value of $Re_{\theta t}$ in the free-stream as function of the turbulence level.

Chapter 3

Methodology

3.1 Geometric configuration

Since the object of the thesis is to assess the behaviour of diffusers at low Reynolds number and the latter scales both with inlet size and bulk velocity ($Re = \bar{U}_1 W_1/\nu$), a small diffuser size was chosen. In particular, the inlet width W_1 is 2 cm, while the diffuser length N is 10 cm. The outlet width W_2 scales with the divergence angle θ, taken as the only parameter for the different simulations. The ratio N/W_1 is 5.

The geometry and the mesh were made using the open-source software *Gmsh* based on the programming language *Python*. By creating a modular geometry and an automatic meshing, it was possible to create a loop scrip to iterate the different simulations in which the iteration variable was the divergence angle. Figures 3.1 and 3.2 represent the geometry used for the simulations, all the geometrical parameters are constant apart from 2θ, which is variable. The corner was modelled as a quadratic Bézier curve with only one control point.

To simulate the plenum exit condition, it was important to define an external chamber, large enough to have the minimum effect on the pressure recovery and flow behaviour. A geometry independence study was performed

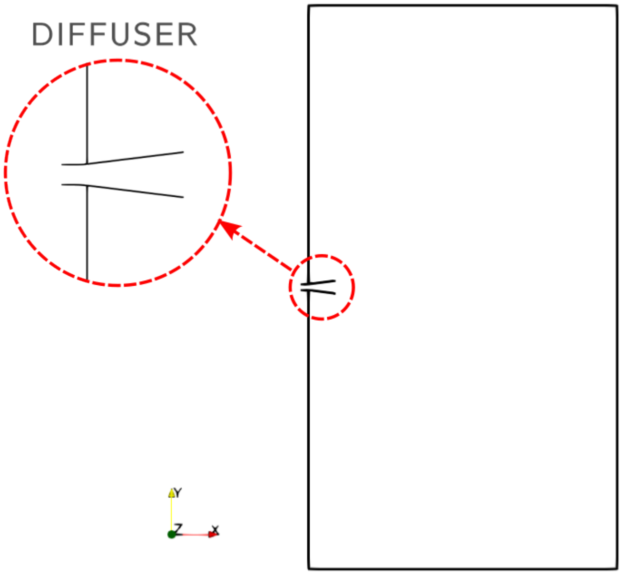

Figure 3.1: Diffuser and external chamber geometry.

to understand the size of this geometric part.

As shown in 3.3, the solution tends to become very unsteady for small sizes, while it is rather stationary if the chamber size increases, due to the fact that the boundary condition is far from the diffuser itself. Figure 3.4 shows the convergence of C_P increasing the external chamber size as expected. Therefore the external chamber was taken of size 50x100 (length and height expressed in diffuser inlet widths) because it is less than 1 percent from the 70x140 case.

3.2 Mesh independence study

Given the geometry explained in the previous paragraph, the mesh consists of a structured grid on the diffuser and an unstructured grid on the external mesh, as shown in Figure 3.5.

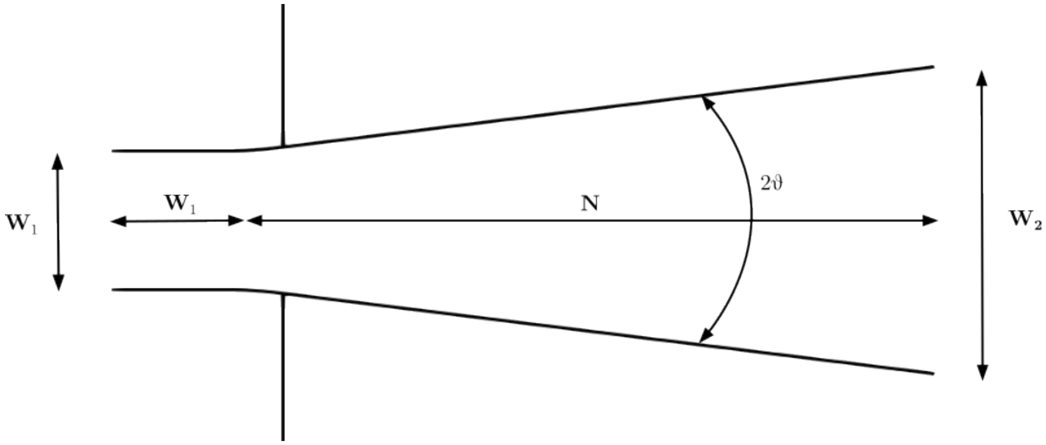

Figure 3.2: Diffuser geometry and its nomenclature.

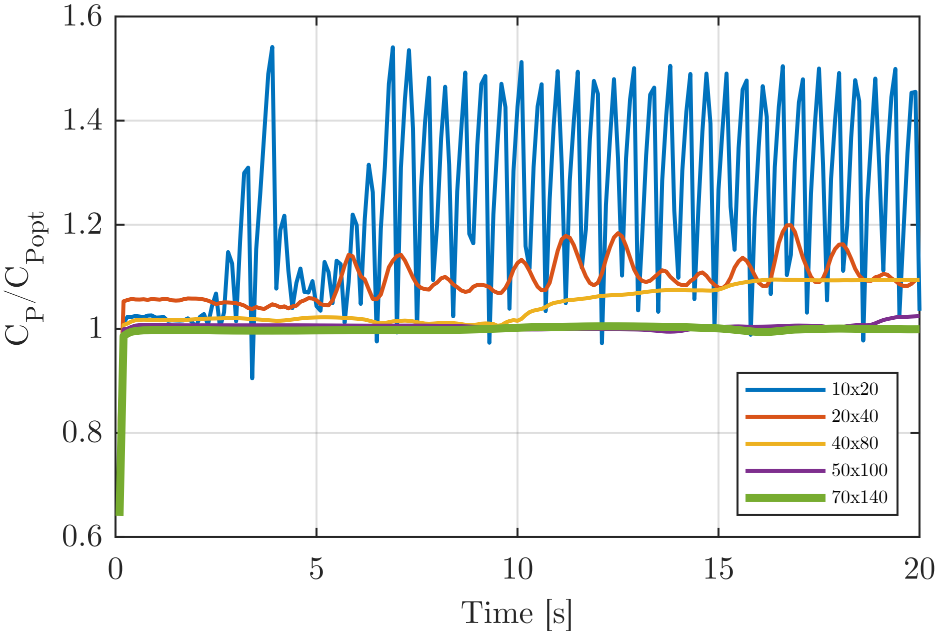

Figure 3.3: C_P series over time with different external chamber sizes, whose length and height are expressed in diffuser inlet widths (W_1). C_{Popt} is the C_P average of the best geometry (70x140).

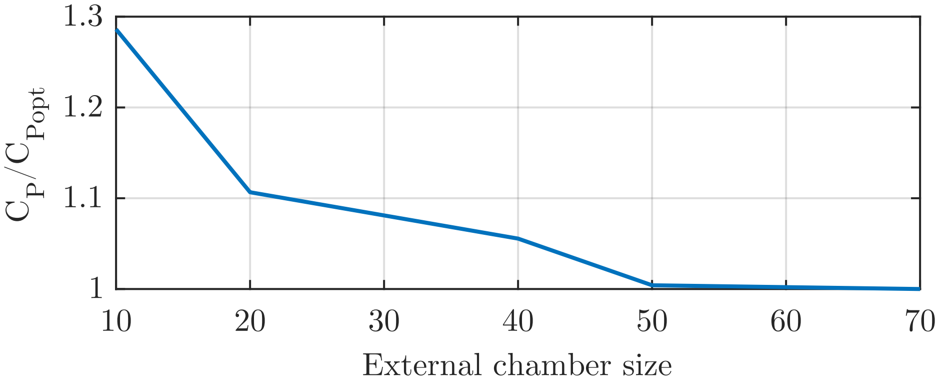

Figure 3.4: Relative C_P averages at different external chamber sizes expressed in diffuser inlet widths. C_{Popt} is the C_P average of the best geometry (70x140).

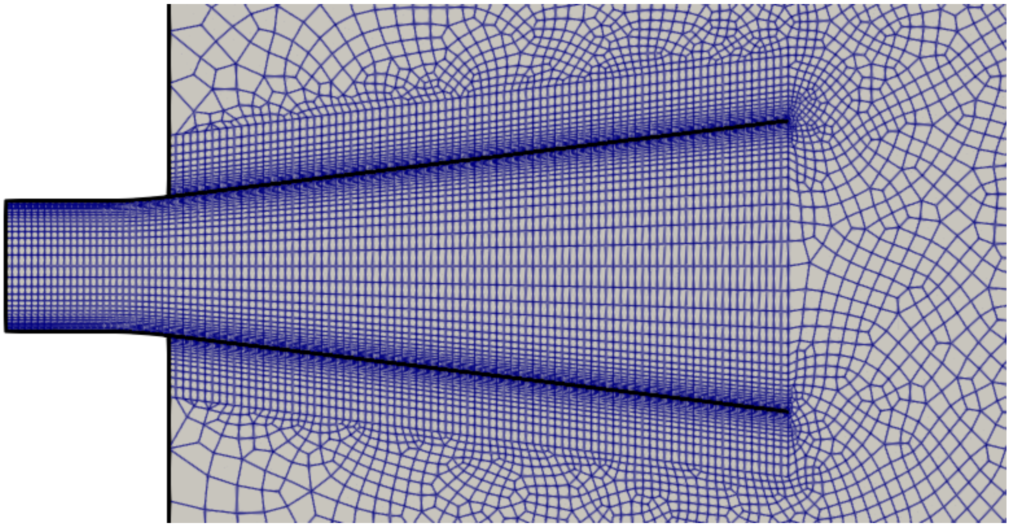

Figure 3.5: Mesh of the diffuser and external chamber.

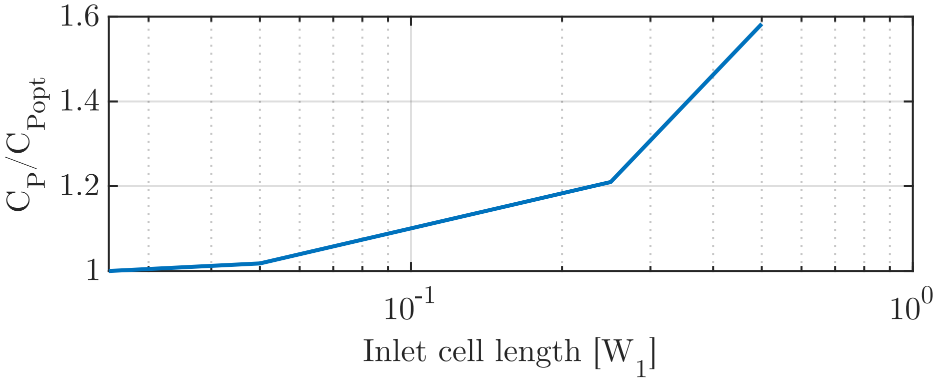

Figure 3.6: Mesh independence study performed on the inlet cell length expressed in diffuser inlet widths (streamwise, x direction, length of the grid cell).

The geometry was meshed using the software *Gmsh*, in which different parameters were considered: the inlet cell length (streamwise, x direction, length of the grid cell at the inlet), the geometric progression coefficients of the streamwise (x direction) cell size of the diffuser, the geometric progression coefficient of the normal (y direction) cell size and finally the plenum mesh size. In order to assess mesh independence, a study was accomplished. Since the mesh is completely modular, as just explained, the single parameters were changed keeping the other constant for a total of four different analyses. The fluid parameter that was kept as a reference is the C_P since it is one of the fundamental variables of the present work. The analysis concerning the inlet cell length is shown in figure 3.6.

All the previous analyses are computed separately, selecting a mesh that would give a C_P within 1 percent from the following finer mesh. Nevertheless, this does not guarantee the error to be within 1 percent once all the parameters are taken into consideration in the single simulation. Therefore, a final simulation of the optimized mesh was compared to the finest mesh in the end and a total error smaller than 2 percent was observed.

After the mesh independence study, the mesh parameters are:

- cell length (x direction) $= 0.05W_1$
- geometric progression in x direction $= 1$
- smallest cell height (y direction) $= 0.005W_1$ ($y^+ \approx 0.5$)
- geometric progression in y direction $= 1.2$

The total number of cells varies between 45000 and 50000 depending on the divergence angle θ.

3.3 CFD model implementation and boundary conditions

As explained earlier, the object of this thesis is to analyse the behaviour of 2D plane diffusers at low Reynolds numbers. Since many simulations were intended to be performed, the only way to maintain a low computational cost was to make use of RANS models. In addition, given a low Reynolds number and a low turbulence level, transition and laminarisation were expected, conducting to the choice of the RANS $k - \omega$ *Transitional SST* model, whose details are explained in the section 2.2.2.

To perform the unsteady RANS simulation, the open-source software OpenFOAM was used, employing the solver PIMPLE. Although many papers perform steady RANS on diffusers, even using the same model of these simulations (for example the work done by Sparrow et al. [18]), for this work was not possible to obtain steady simulations in a reasonable time because of the unsteady nature of the flow, probably accentuated by the plenum exit condition.

A total simulation time of 5.5 seconds was considered, after analysing some simulations performed during the grid convergence analysis. The time is considered as a sum of a first transient time of 0.5 seconds corresponding to $30t$ (where $t = N/\bar{U}_1$ is the characteristic time scale of the diffuser) and a following time of 5 seconds corresponding to $300t$, in which data is time-averaged.

As boundary conditions, a velocity profile at the inlet and no slip at the wall were imposed, while concerning the external chamber, static pressure and no shear were imposed respectively at the outlet and at the wall.

In the $k-\omega$ *Transitional SST* model, the turbulence kinetic energy k, the specific turbulence dissipation rate ω, the intermittency γ and the $\hat{Re}_{\theta t}$ boundary conditions must be specified besides velocity and pressure.

The following equations were exploited in defining the boundary conditions at the inlet:

$k = 1.5(UI)^2 \qquad \omega = \sqrt{k}/l$

where l is the turbulence length scale defined as $l = 0.038D$ for fully developed channel and pipe flows (D is the hydraulic diameter) or $l = 0.22\delta$ (δ is the boundary layer thickness) in case of generic wall-bounded flows.

As explained in section 2.2.2 for the intermittency variable γ, a value of 1 was imposed at the inlet, while for $\hat{Re}_{\theta t}$ the equations 2.25 were exploited.

The Reynolds number was chosen according to the critical Reynolds in fully developed channel flow, in order to simulate a flow that is very close to transition, as may happen to small-size diffusers operating at relatively low velocities. Sano and Tamai [19] found a critical Reynolds number of 7696 ($Re = \bar{U}W_1/\nu$) for fully developed Poiseuille flow, which is why $Re = 8163$ was chosen for the following simulation to ensure a turbulent inlet profile close to transition. This means that the bulk velocity $\bar{U_1}$ is 6 m/s. Considering the same bulk velocity for all the different velocity profiles, the maximum velocity changed accordingly.

Three different inlet velocity profiles and three different turbulence levels were chosen (all the other parameters like k and ω are changed accordingly), for a total of nine cases. For each case, different divergence angles θ were simulated in order to offer a complete characterization of 2D planar diffusers, considering the most influencing parameters. Pressure recovery and outlet velocity profiles were the primary parameters analysed in these simulations. The turbulence levels are 10, 3 and 0.05 percent, representing a high, a medium and a very low turbulence intensity, respectively. For the inlet velocity profile, a generalised power law equation was used, following the one proposed by Salama [20]:

$$\frac{U}{U_{max}} = \left[1 - \left(\frac{y}{W_1}\right)^m\right]^{\frac{1}{n}} \tag{3.1}$$

where m and n are two coefficients function of the Reynolds number.

This equation is not suitable for accurate analysis of the wall shear stress, where the famous logarithmic law of the wall is more accurate; nevertheless, equation 3.1 can be exploited in a RANS model.

Coefficients m and n were determined from experimental data interpolations, and they vary based on the flow regime and Reynolds number. When $m = 2$ and $n = 1$, the fully developed channel flow velocity profile corresponds to a fully developed laminar channel flow. Salama [20] established that a fully developed turbulent flow has coefficients: $m = 2$ and $n = 12$. The different velocity profiles can be described by means of the blockage factor B, defined in Equation 2.5. In the present work, the three velocity profiles are:

- tophat: $B = 0$
- turbulent profile (m = 2, n = 12): $B = 0.05$
- laminar profile (m = 2, n = 1): $B = 0.33$

Figure 3.7 represents the three velocity profiles.

Since the bulk velocity $\bar{U}$ is fixed for all profiles, the maximum velocity U_{max} was obtained by Equation 2.5, after having defined coefficients m and n.

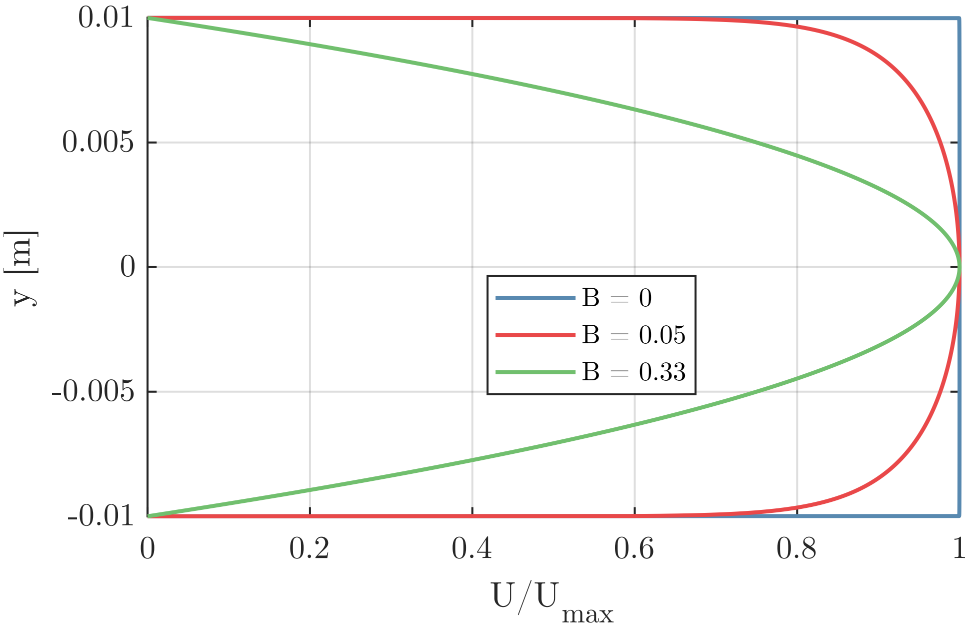

Figure 3.7: The three different velocity profiles at the diffuser inlet.

Chapter 4

Results and discussion

4.1 Model validation

To validate the computational model, different simulations were performed, following the assumption of the experimental data provided by Reneau et al. [2]. In particular, the geometry was not changed with respect to the one explained in chapter 3. Still, the flow conditions were changed in order to ensure a high turbulent flow and an inlet blockage factor suitable for a comparison with the data available in the above-mentioned research work.

The Reynolds number of the experimental data was above $5 * 10^5$. Therefore a value of $1 * 10^6$ was chosen, ensuring a fully turbulent boundary layer. Following the paper conditions, a turbulence intensity of 2 percent was selected, and a tophat velocity profile was imposed as boundary condition at one throat length upstream of the diffuser inlet, to ensure an inlet blockage factor of 0.007.

Experimental data provided by Reneau et al. [2] are given by a chart made by interpolating several experiments of diffusers of different geometries (two-dimensional with different divergence angles and N/W_1 ratios). Since the chart represents different experiments from different setups, the geometry (e.g. the fillets between the inlet duct and the diffuser, and the surface

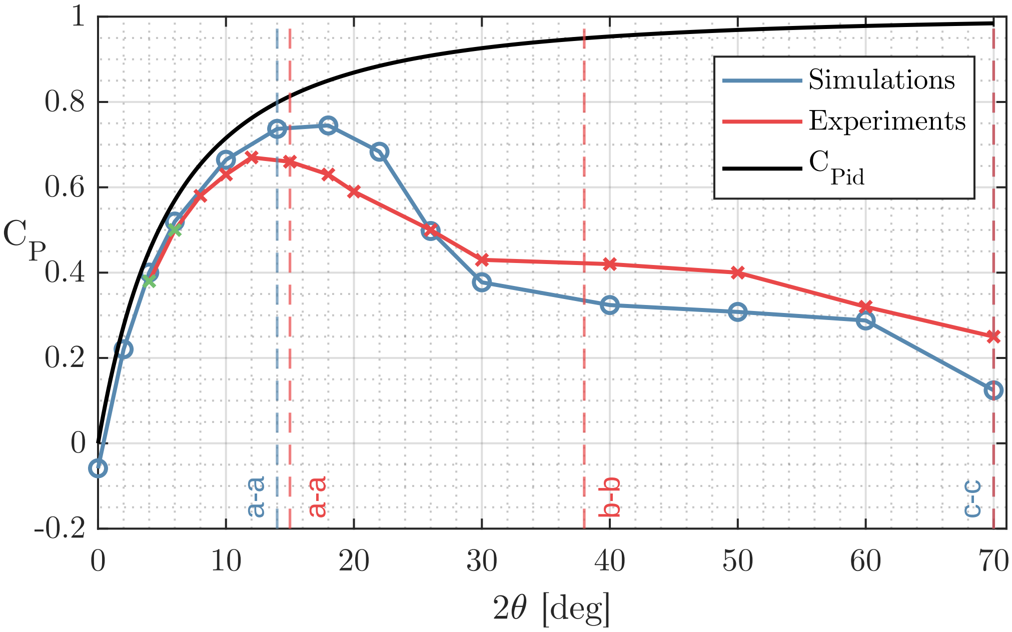

Figure 4.1: Comparison of pressure recovery coefficients between simulations and experimental data [2], varying the divergence angle. $Tu = 2\%$, $B = 0.007$. The green points were deduced from the interpolation curve of $B = 0.015$. The dashed lines represent the angles of the stall regimes as expressed in Figure 2.5: a-a for the Large Transitory stall, b-b for the Fully-Developed two-dimensional stall, c-c for the Jet Flow.

roughness) and the flow conditions could slightly change among the several tests. This uncertainty (estimated at less than 6 percent [2]) has to be summed to the uncertainty of visually retrieving the pressure recovery curve from the chart starting from the N/W_1 ratio (5 in this case).

It should be remarked that the RANS model used for these simulations is the same one as the one used for all the other simulations of the present thesis, namely the $k{-}\omega\ SSTLM$ model. However, operating at a very high Reynolds number, this model coincides with the classical $k-\omega\ SST$ model since the boundary layer is completely turbulent. This was the only validation possible because, as explained earlier, the literature does not present any experimental data involving diffusers which operate with a laminar boundary layer.

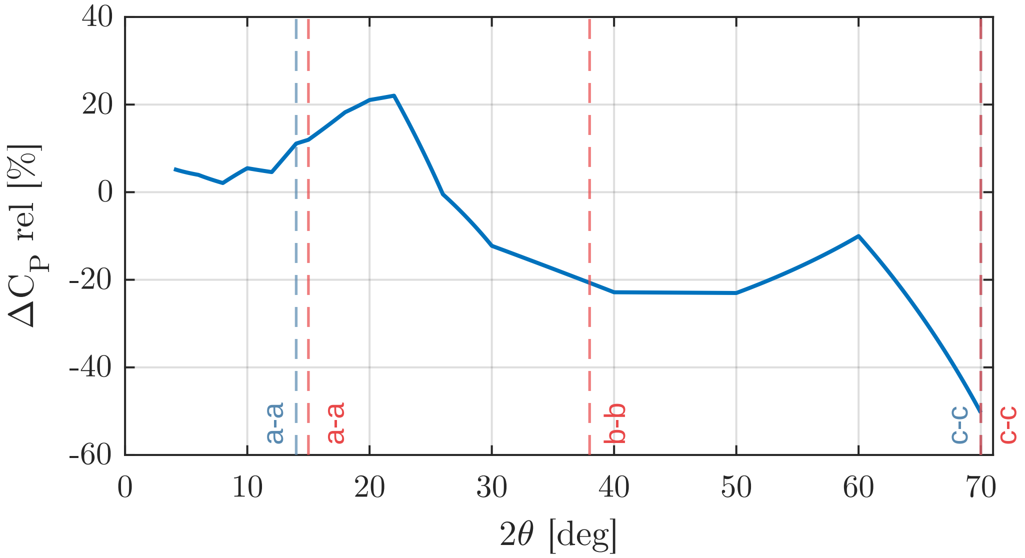

Figure 4.2: Relative error of the linear interpolation of the pressure recovery coefficients between simulations and experimental data [2], varying the divergence angle. $Tu = 2\%$, $B = 0.007$. The dashed lines represent the angles of the stall regimes as expressed in Figure 2.5: a-a for the Large Transitory stall, b-b for the Fully-Developed two-dimensional stall, c-c for the Jet Flow.

Observing Figure 4.1, it can be noticed that below $2\theta = 12°$ the simulations are very consistent with the experimental data. Nevertheless, simulations tend to overestimate the pressure recovery peak and its angle by 10 percent. At the pressure recovery peak of the simulations, there is a 15-20 percent of overestimation. In correspondence to the fully developed two-dimensional stall, there is an inversion of the previous trend, with an underestimation of the pressure recovery with respect to experimental data (30 percent). Finally, the pressure recovery curves tend to converge before the jet flow regime. The simulation can accurately detect the angle at which the jet flow regime appears, but it tends to underestimate the pressure recovery by a considerable amount at $2\theta = 70°$ (50 percent). From the simulations, a clear distinction between the large transitory stall and the fully-developed two-dimensional stall is not present because analyses of the velocity fields do not show stalls that build up and are washed out. The flow attaches to a divergence wall at the correct angle but no unsteadiness is present, unlike the experiments.

Figure 4.2 represents the difference in pressure recovery between experimental data and simulation, which clearly remains below ±0.15.

In conclusion, considering the very strong dependency of data on inlet conditions, it is fairly impossible to simulate the flow with the same inlet conditions of experimental data. A small variation of turbulence intensity or velocity profile can have a strong impact on the pressure recovery. Geometrical parameters such as the fillet at the throat can have an important effect, which remains unclear today. Nevertheless, it is possible to understand the trend of the pressure recovery curve and this seems to correspond well with experimental data.

As explained earlier, a total of nine RANS cases have been performed, each of them with a varying number of simulations, depending on the divergence angle range.

Results will be presented first by analysing the flow profiles and conditions at the outlet and then by comparing the pressure recovery coefficient and effectiveness for the different turbulence intensities.

4.2 Diffuser outlet analysis

Figures 4.3, 4.4 and 4.5 show the velocity profiles at the diffuser outlet for all the simulations, split into the three turbulence intensity cases. It can be seen that the flow tends to attach to a diverging wall after the maximum pressure recovery (which curves are shown in Figures 4.7, 4.8 and 4.9), compatible with a transitory stall regime. The main difference from the descriptions given by Reneau et al. [2] is that no unsteadiness is present; therefore, the flow is completely attached to a diverging wall as it is supposed to be, having $N/W_1 = 5$, but the other wall does not present the stall regions that repeatedly build up and are subsequently washed out of the diffuser. Indeed, a transitory analysis of the flow reveals that no strong unsteadiness is present. The model can detect recirculation bubbles, but they are steady, even using an unsteady model.

It is useful to analyse the uniformity of the flow at the diffuser outlet for the different turbulence intensities and velocity profiles. The flow uniformity index of Equation 2.4 was exploited. Figure 4.6 shows the value of γ for the different simulations and illustrates that γ tends to a defined value in the case of jet flow regime, at least for the turbulence intensities of 3 and 10 percent. In addition, the flow uniformity index monotonically decreases increasing the divergence angle 2θ. Despite a relatively uniform decrease of γ, the higher rate of drop is in correspondence with the maximum pressure recovery and therefore in the large transitory stall regime.

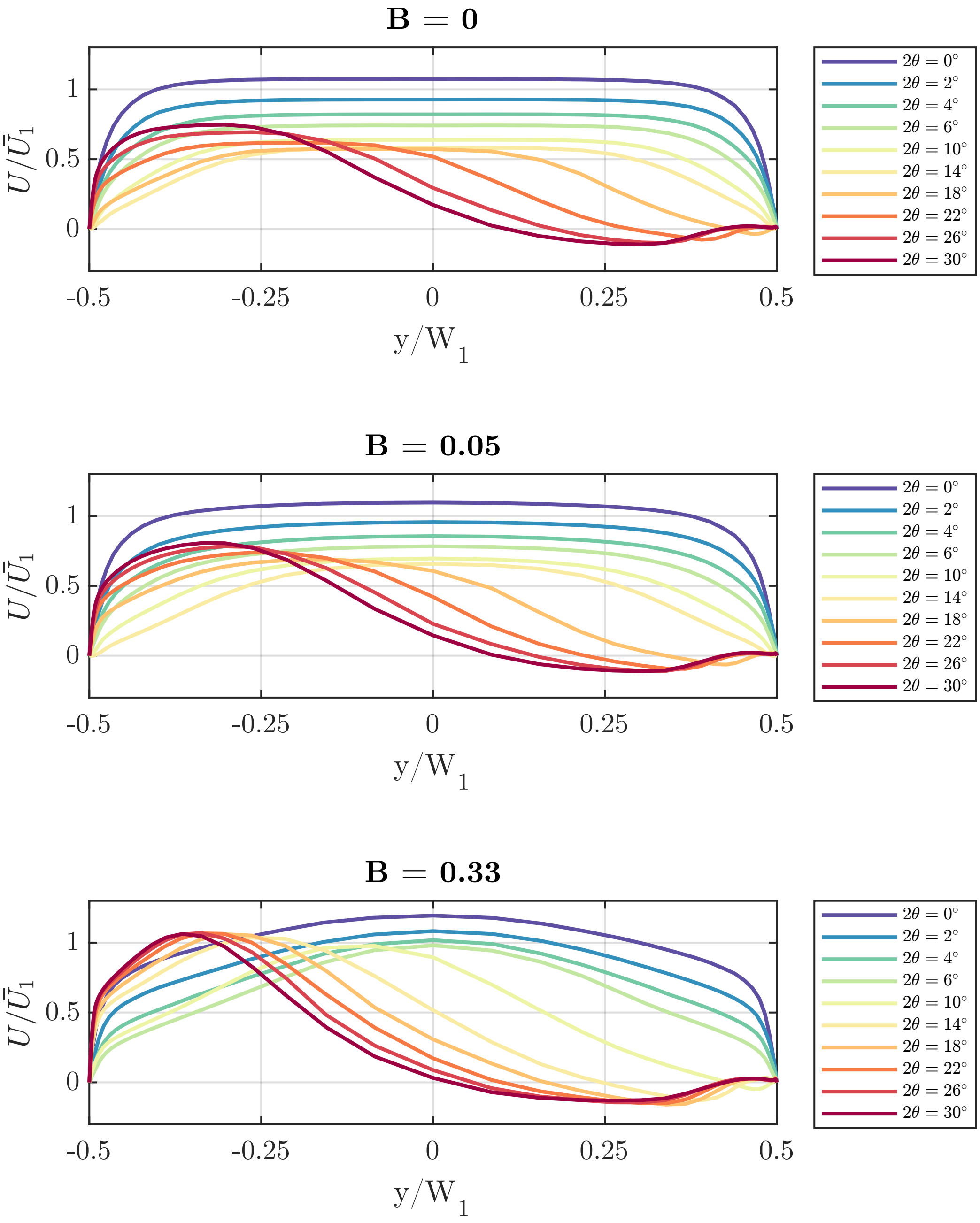

Figure 4.3: Velocity profiles at the diffuser outlet at the time instant $t = 5.5s$, for the three inlet blockage factors, and $Tu = 10\%$.

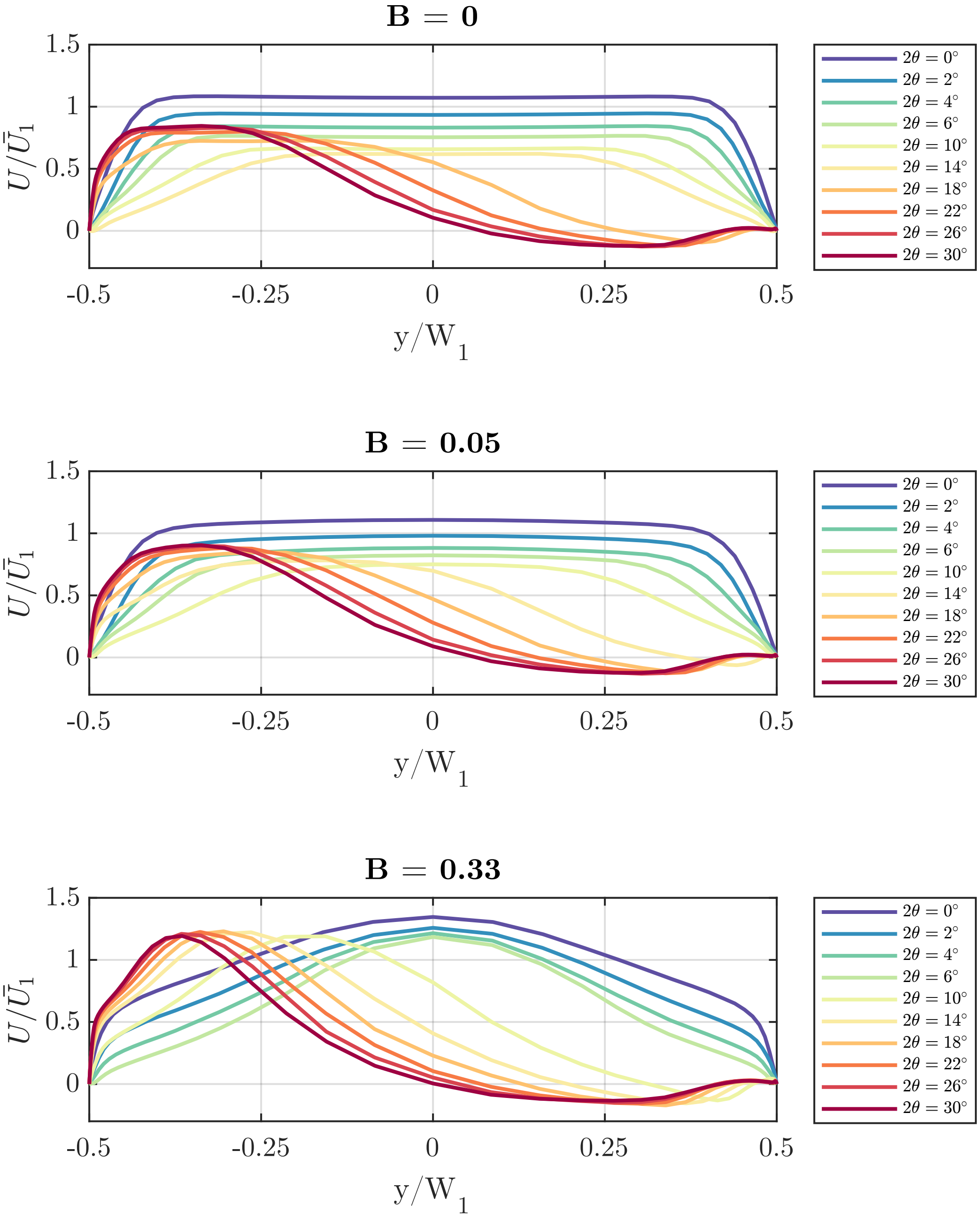

Figure 4.4: Velocity profiles at the diffuser outlet at the time instant $t = 5.5s$, for the three inlet blockage factors, and $Tu = 3\%$.

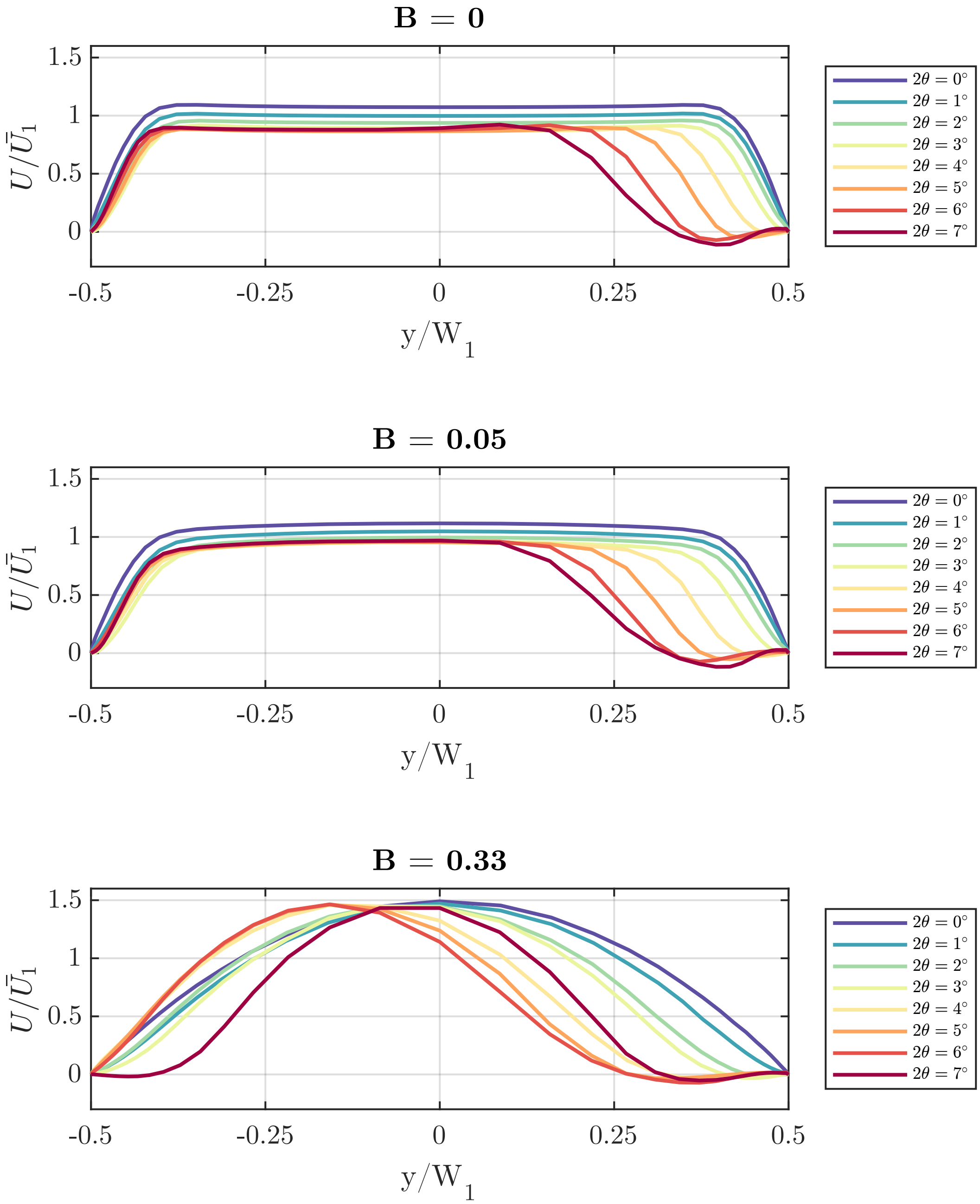

Figure 4.5: Velocity profiles at the diffuser outlet at the time instant $t = 5.5s$, for the three inlet blockage factors, and $Tu = 0.05\%$.

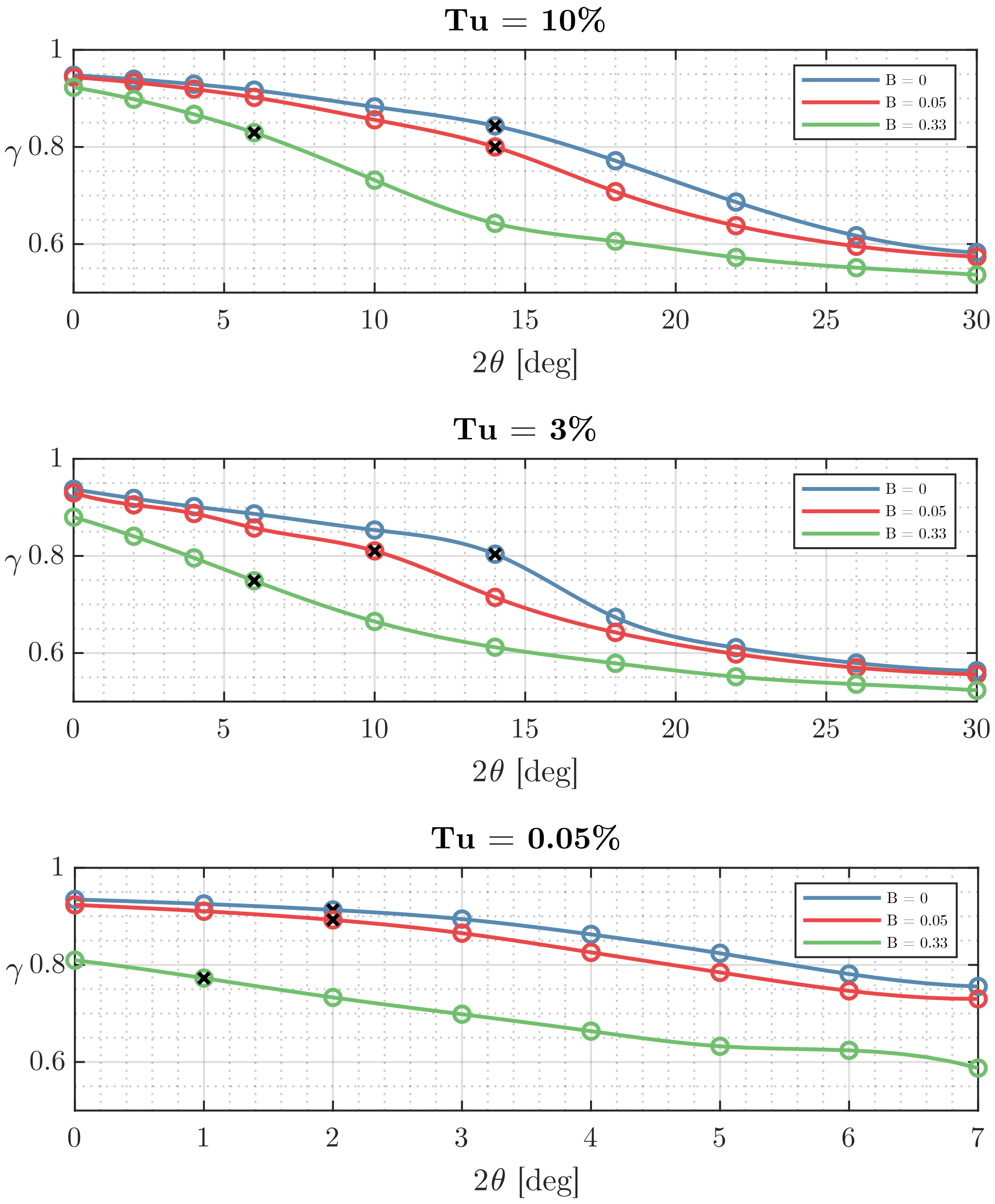

Figure 4.6: Flow uniformity index γ for the three turbulence intensity cases. At every turbulence level, the correspondent simulation with the highest angle at which the flow is attached is marked with a black cross.

4.3 Turbulence intensity: 10 percent

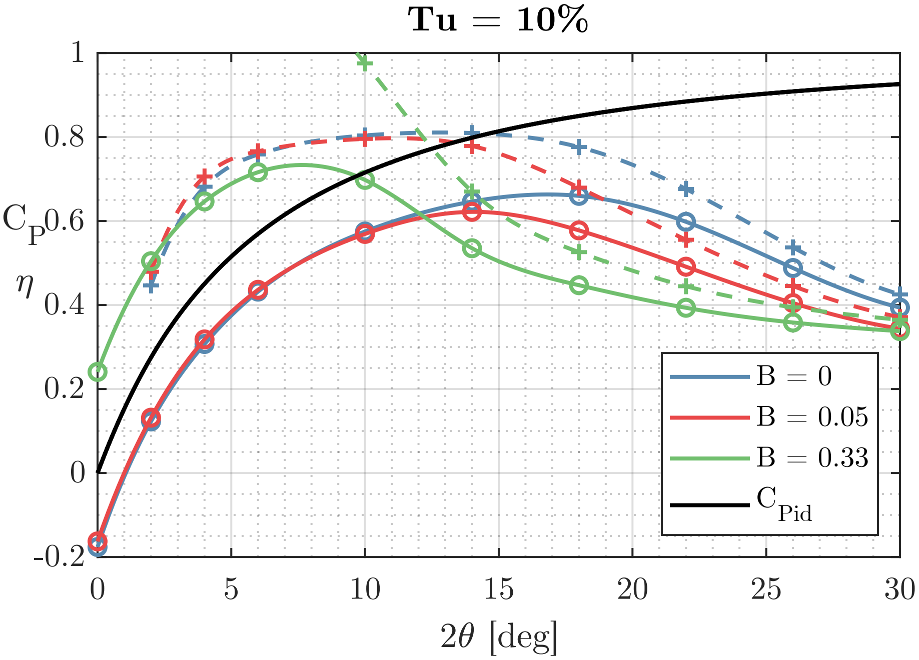

Figure 4.7: C_P (continuous line) and η (dashed line) at different inlet blockage factors (inlet velocity profiles) for Tu = 10%.

Figure 4.7 shows the C_P and η for a turbulence intensity equal to 10 percent, corresponding to a high turbulence level. The boundary layer is forced to be turbulent due to the high turbulence intensity and by analysing the intermittency variable γ, we conclude that there is no laminarisation.

As expected from experimental data on diffusers with a turbulent boundary layer available in literature [2], the maximum pressure recovery is obtained for $B = 0$, while increasing displacement thickness ($B = 0.05$), a decrement of C_P is shown, as well as the angle of maximum C_P.

At the same time, a slight increase of C_P can be noted at lower angles, where the flow is completely attached, for B increasing from 0 to 0.05. This trend becomes apparent when $B = 0.33$. In this case, the maximum pressure recovery occurs at very low divergence angles ($2\theta \approx 8°$). Furthermore, the C_P is 0.73, and therefore greater than in the previous cases.

It can be noted that the case of $B = 0.33$ is the only one to have a pressure recovery greater than 0 when the diverging angle is null (corresponding to a channel flow into a stationary atmosphere). This behaviour is well known and will be later explained in detail in section 4.6.

4.4 Turbulence intensity: 3 percent

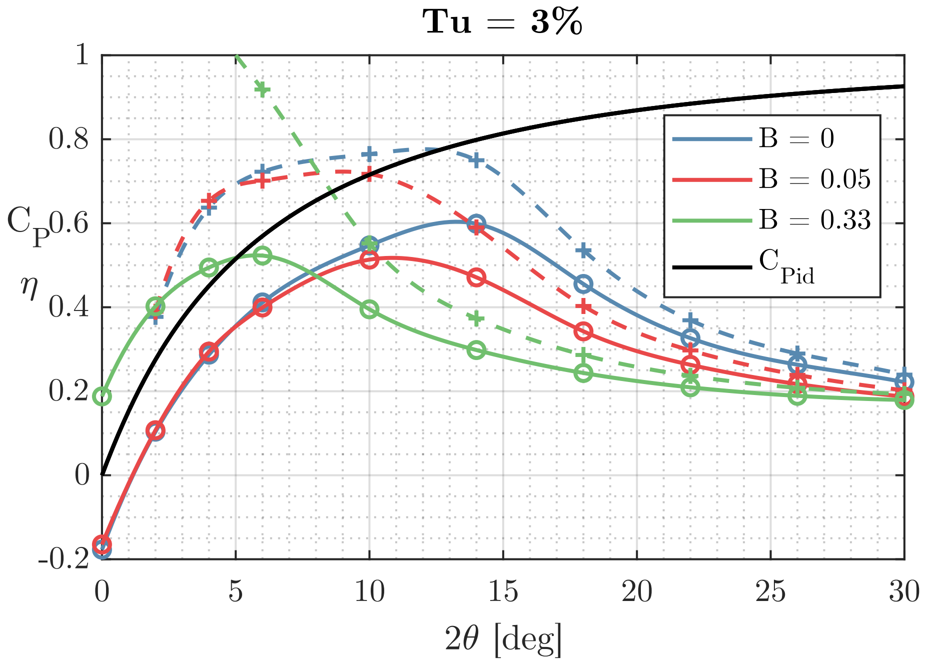

Figure 4.8: C_P (continuous line) and η (dashed line) at different inlet blockage factors (inlet velocity profiles) for Tu = 3%.

The case of a turbulence intensity of 3 percent does not differ significantly from the case of a turbulence intensity of 10 percent. The major differences are the reduced pressure recovery for all blockage factors as well as their angle of maximum pressure recovery. Effectiveness decreases as a consequence of smaller pressure recovery. As in the previous case, the effectiveness is greater than 1 for $B = 0.33$, which will be explained in section 4.6 as well.

4.5 Turbulence intensity: 0.05 percent

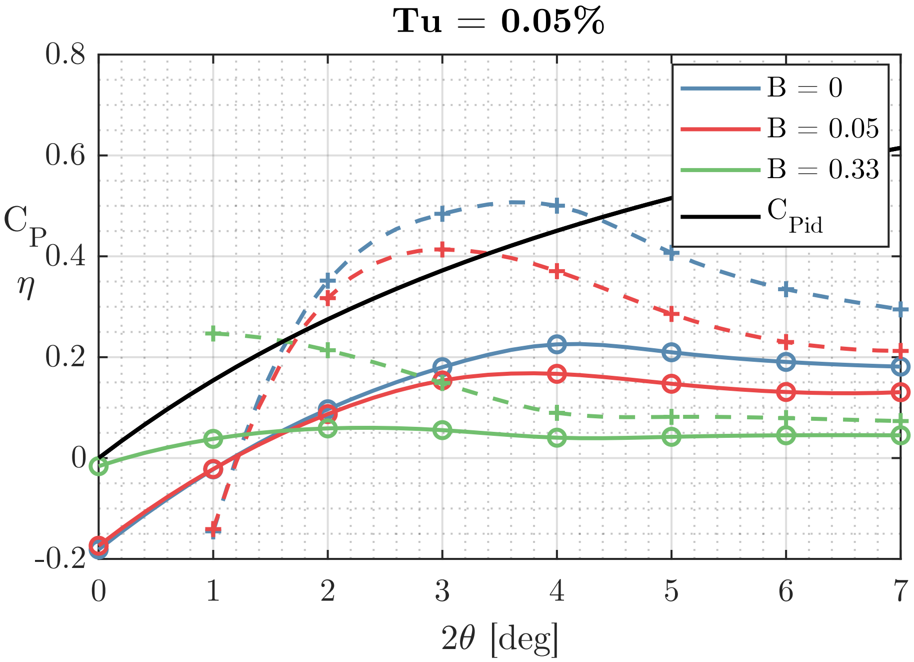

Figure 4.9: C_P (continuous line) and η (dashed line) at different inlet blockage factors (inlet velocity profiles) for Tu = 0.05%.

The pressure recovery is very low in the case of a turbulence intensity of 0.05 percent, mostly for higher blockage factors. Indeed, the maximum C_P does not increase for higher blockage factors, unlike in the previous cases with higher turbulence intensity. The angles of maximum pressure recovery are very small and therefore the range of angles at which simulations were performed differs from the previous cases.

When the divergence angle is null, it is not possible to observe any pressure recovery, even though for $B = 0.33$ the pressure drop is significantly lower than the cases of $B = 0$ and $B = 0.05$. The increment of C_P for $B = 0.33$ at low diverging angles will be explained in the following section.

4.6 Modified effectiveness

As established previously, when the blockage factor is high, the diffuser tends to recover static pressure even in the presence of a null diverging angle. As Tyler and Williamson [21] explained in 1967, this happens because of diffusion, which tends to make the flow uniform at the outlet. In fact, due to a non-uniform inlet velocity profile, the flow is more energetic and the dynamic pressure takes the following form:

$$\bar{q_1} = \frac{1}{2}\alpha\rho\bar{U_1^2}, \quad where\,\alpha = \frac{\int_0^{W_1} U_1^3 dy}{\bar{U}_1^3 A} \tag{4.1}$$

α is the velocity profile energy coefficient and it results in 1 when the flow profile is completely uniform (tophat).

Therefore, in the case of a null divergence angle, the total pressure does not increase through the diffuser, even if the static pressure increases and the bulk velocity remains constant because the flow becomes more uniform and the dynamic pressure decreases.

To take this behaviour into consideration, Tyler and Williamson [21] exploited a parameter called modified effectiveness ($\bar{\eta}$). The modified effectiveness is always smaller or equal to 1, and therefore it guarantees a more robust parameter to characterise diffusers at high blockage factors.

The new C_{Pid} considered in the modified effectiveness takes the form of $\overline{C_{Pid}} = (DF)_1^2 - 1/(AR)^2$, where (DF) is the distortion factor at the diffuser inlet, expressed as $(DF)_1 = U_{1max}/\bar{U_1}$. The distortion factor is linked to the blockage factor B by the following relation: $B = 1 - 1/(DF)$.

The modified effectiveness is:

$$\bar{\eta} = \frac{C_P}{\overline{C_{Pid}}} = \frac{C_P}{(DF)_1^2 - \frac{1}{(AR)^2}} \tag{4.2}$$

It can be observed that in the case of a uniform inlet flow, the modified effectiveness reverts to the original effectiveness form, while it is smaller than η in the case of a non-uniform inlet flow.

Following the derivations proposed by Kline et al. [1], a similar approach can be exploited to determine where the maximum modified effectiveness is located. Given the expression of η and differentiating it with respect to θ to find the maximum, the following equation is obtained:

$$\frac{1}{C_P}\frac{\partial C_P}{\partial \theta} = \frac{1}{C_{Pid}}\frac{\partial C_{Pid}}{\partial \theta} \tag{4.3}$$

A similar equation can be obtained by differentiating the expression of $\bar{\eta}$ (Equation 4.2):

$$\frac{1}{C_P}\frac{\partial C_P}{\partial \theta} = \frac{1}{\overline{C_{Pid}}}\frac{\partial \overline{C_{Pid}}}{\partial \theta} \tag{4.4}$$

Following the same reasoning that Kline et al. [1] used for η_{max}, $\bar{\eta}_{max}$ should also always be smaller than C_{Pmax} because in the Equation 4.4, C_P, $\overline{C_{Pid}}$ and $\partial\overline{C_{Pid}}/\partial\theta$ are always positive by definition. Therefore, to maintain the equality, $\partial C_P/\partial\theta$ must also be positive and the angle of C_{Pmax} is located after $\bar{\eta}_{max}$.

To understand if $\theta(\bar{\eta}_{max})$ is greater or smaller than $\theta(\eta_{max})$, Equations 4.3 and 4.4 can be exploited. It can be noted that $\overline{C_{Pid}}/\partial\theta$ is always equal to $\partial C_P/\partial\theta$ because the distortion factor DF is not a function of θ. Furthermore, $\overline{C_{Pid}}$ is always greater than C_{Pid} if $DF > 1$ (when $B > 0$). This means that the angle of $\bar{\eta}_{max}$ is located after the angle of η_{max} but before the angle of C_{Pmax}.

In Figure 4.10 the modified effectiveness is plotted for the different turbulence intensity cases. It is important to notice that $\bar{\eta}$ does not exceed 1, while η does, since $C_P > C_{Pid}$ for high blockage factors, as visible in Figures 4.7 and 4.8.

Figure 4.11 shows the different blockage factors at the outlet for the different turbulence levels and inlet velocity profiles. Data is available till backflow appears at the outlet. From these plots, it is clear that in the case of a laminar boundary layer, there is no turbulent diffusion, hence the blockage factor at the outlet is almost the same as the inlet, and the flow maintains its kinetic energy. This can be observed in the values of the blockage factor at the outlet in the case of $B = 0.33$ for the different turbulence intensities. In the case of a turbulence level of 10 percent, B_2 is 0.163; for a turbulence level of 3 percent, B_2 is 0.26, and finally, for a turbulence level of 0.05 percent, B_2 is 0.33.

As explained earlier, from Figure 4.10 and Table 4.1, it can be concluded that the angle of maximum modified effectiveness is always greater than the angle of maximum effectiveness (apart from the case of $B = 0$, when they coincide), while it is always smaller than the angle of maximum pressure recovery.

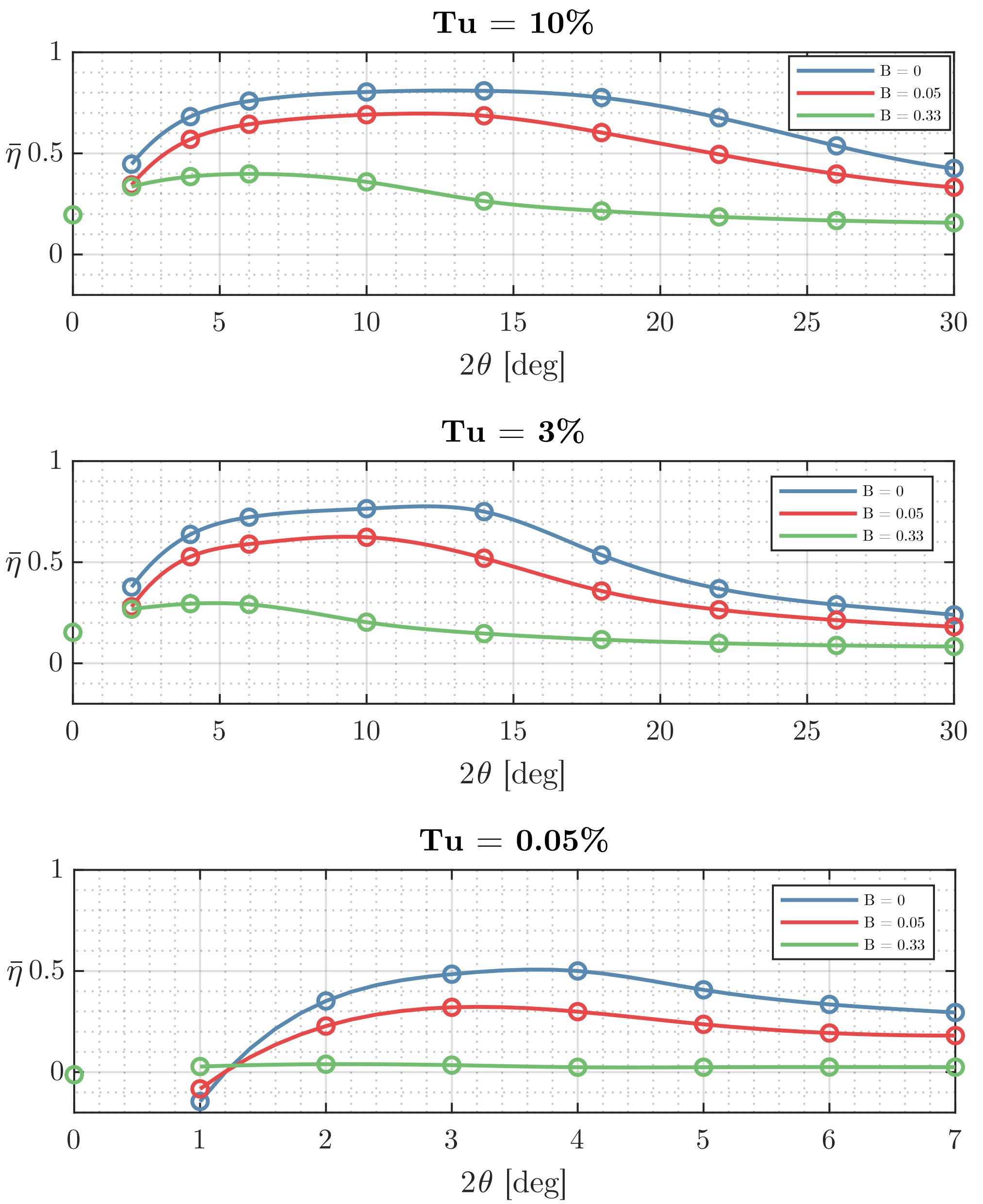

Figure 4.10: Modified effectiveness $\bar{\eta}$ for the three turbulence intensity cases.

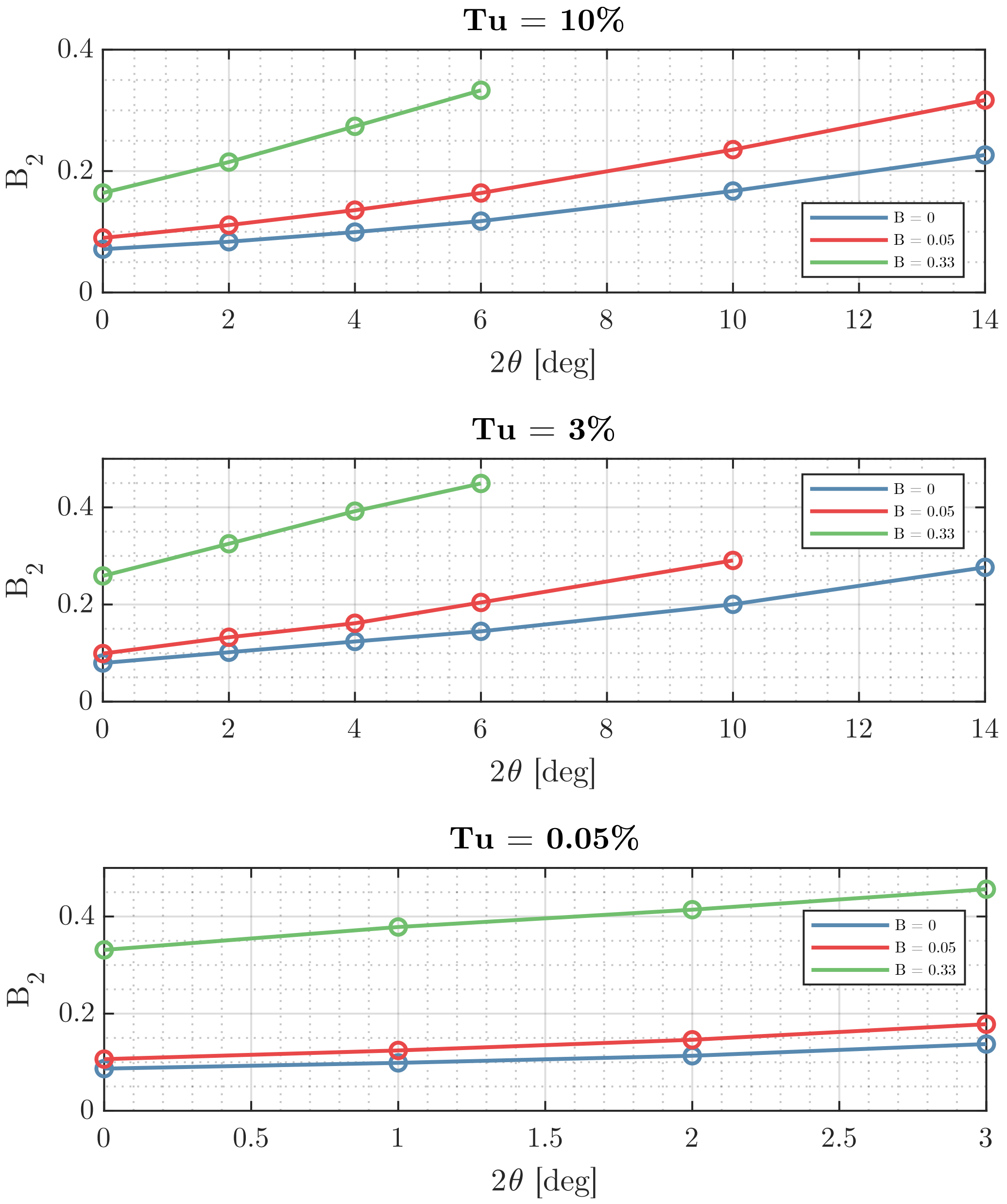

Figure 4.11: Blockage factor at the diffuser outlet for the three turbulence intensity cases.

(a) Tu = 10 %

	C_{Pmax}	η_{max}	$\bar{\eta}_{max}$	$2\theta(C_{Pmax})$	$2\theta(\eta_{max})$	$2\theta(\bar{\eta}_{max})$
$B = 0$	0.66	0.81	0.81	16.8	12.8	12.8
$B = 0.05$	0.62	0.80	0.70	14.0	11.2	11.8
$B = 0.33$	0.73	/	0.40	7.6	/	6.0

(b) Tu = 3 %

	C_{Pmax}	η_{max}	$\bar{\eta}_{max}$	$2\theta(C_{Pmax})$	$2\theta(\eta_{max})$	$2\theta(\bar{\eta}_{max})$
$B = 0$	0.60	0.78	0.78	13.2	12.0	12.0
$B = 0.05$	0.52	0.72	0.63	10.8	9.0	9.4
$B = 0.33$	0.52	/	0.30	5.8	/	4.8

(c) Tu = 0.05 %

	C_{Pmax}	η_{max}	$\bar{\eta}_{max}$	$2\theta(C_{Pmax})$	$2\theta(\eta_{max})$	$2\theta(\bar{\eta}_{max})$
$B = 0$	0.23	0.51	0.51	4.2	3.6	3.6
$B = 0.05$	0.17	0.41	0.32	3.8	3.0	3.2
$B = 0.33$	0.06	0.25	0.04	2.4	1.0	2.2

Table 4.1: Maximum value of C_P, η and $\bar{\eta}$ and their corresponding divergence angle 2θ, for the different turbulence intensity cases.

Table 4.1 shows the maximum values for C_P, effectiveness and modified effectiveness with their corresponding angle 2θ. It should be pointed out that the highest values of C_P, η and $\bar{\eta}$ are found for the highest turbulence intensity. The highest angles of these maximum values correspond to the same case. Between the turbulence intensities of 10 and 3 percent, there is a difference in performance, but it is not as relevant as the corresponding difference between 3 and 0.05 percent.

Therefore, to recapitulate, two main factors do not allow a high pressure recovery for diffusers operating with a laminar flow. The first reason is that the laminar boundary layer tends to separate very early, and the second reason is that the lack of turbulent diffusion cannot make the flow uniform through the diffuser. These two factors are dependent, because the lack of diffusivity cannot avoid an early separation. This is particularly visible in the case of $B = 0.33$, because both factors affect the pressure recovery, leading to $C_{Pmax} = 0.06$.

It is important to point out that the modified effectiveness assumes an important role even for low blockage factors. Indeed, for the case of $B = 0.05$, there is more than a 10 percent difference between the original and the modified effectiveness.

Chapter 5

Conclusions and future work

5.1 Conclusions

Different CFD simulations were performed in order to assess the behaviour of two-dimensional diffusers operating at a low Reynolds number with different inlet conditions and with a plenum exit condition. Three different turbulence intensities were varied, in particular 10 percent, 3 percent and 0.05 percent, thus ranging from a completely turbulent to a laminar inlet velocity profile.

In addition, three different inlet displacement thicknesses were studied, utilising the adimensional blockage factor, employed by varying the inlet velocity profile for which a modified power law was used.

The only geometrical parameter to change was the divergence angle 2θ.

As in the case of a high Reynolds number [2], it can be asserted that even in the presence of a low Reynolds number, inlet conditions play an important role in determining the pressure recovery of the diffuser. The main reason is that flow tends to laminarise easily, which leads to early separations and results in an important sensitivity to inlet condition, probably even more emphasised than the high Reynolds number case.

This sensitivity is mostly valid for all the diffusers that present a very short inlet channel before the diverging walls. In fact, if the channel is sufficiently long, a fully developed flow can be established at the diffuser inlet, hence the blockage factor and the turbulence intensity are less affected by the conditions at the inlet of the channel.

From the results of the simulations of the present geometry, which presents a very short channel (the length is equal to the width), five main conclusions can be asserted:

- For diffusers operating at high Reynolds numbers, the $k{-}\omega$ *Transitional SST* model, operating as the $k-\omega$ *SST* model, predicts the pressure recovery with respect to experimental data [2] fairly well, with an absolute error of the C_P within ± 0.15 throughout the range of divergence angles from 0 to 70 degrees.
- For diffusers operating at low Reynolds numbers, assessing the turbulence level is fundamental to understand the pressure recovery, which can considerably vary between a medium (3 percent) and a high (10 percent) turbulence intensity. The difference is almost 10 percent for $B = 0$ and it increases up to 30 percent and more for $B = 0.33$. It is reasonable to think that the difference can further increase in case of higher blockage factors.
- For a turbulence intensity of 0.05 percent, corresponding to a laminar flow, the pressure recovery is considerably low (0.23 for the tophat velocity profile), mostly due to early laminar separation. This substantially reduces the value of the divergence angle at which the stall appears. Indeed the maximum pressure recovery is at a total included angle (2θ) of 4.2 degrees instead of 13.2 and 16.8 for $Tu = 3\%$ and $Tu = 10\%$, respectively.
- In the case of a high blockage factor, 0.33 for the simulations performed here, the use of modified effectiveness $\bar{\eta}$ (explained in section 4.6) is fundamental to take into account the additional dynamic pressure that the inlet flow presents. Even for $B = 0.05$, there is a substantial

difference of more than 10 percent in comparison to the classical η formulation. Furthermore, the angle of maximum effectiveness loses its significance and is misleading for high blockage factors because it tends to $2\theta = 0°$. The angle of maximum modified effectiveness should be used instead, and it was shown to be between the angle of maximum effectiveness and maximum pressure recovery.

- Concerning the analysis of the velocity profiles at the outlet, the stall patterns seem to be very similar between the different turbulence intensities, apart from the angles at which the stall appears. The unsteadiness of the transitory stall is not visible either from the velocity profiles at the outlet or from the total flow field visualisation through the simulation time. In any case, the mean flow velocity profiles seem to be well predicted.

5.2 Future work

In order to assess the validity of the RANS model used in this thesis, namely the $k - \omega$ *Transitional SST*, an experimental setup was considered. This would also allow us to characterise the different two-dimensional diffusers in a more general way, by the use of pressure taps or flow visualisation.

Diffusers can be designed and 3D printed to match the outlet of a blowing-type wind tunnel in which velocity and therefore Reynolds number can be changed as desired. The diffuser can discharge directly in a stationary atmosphere or a tail channel can be mounted at the end of the diverging walls. Experimental data can be acquired at the outlet using hot-wire anemometers, in order to analyse the velocity profile and the different stall regimes associated with the divergence angle and inlet conditions. Pressure recovery can be obtained by using pressure taps.

If the diffuser is made exploiting transparent walls, flow visualisation can

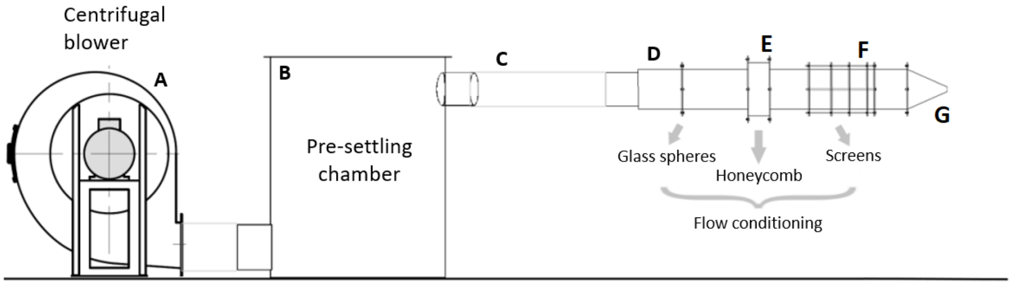

Figure 5.1: Side view schematic of planar jet wind tunnel. Flow is generated by a centrifugal blower (A), transferred to the pre-settling chamber (B), and then to the rectangular prism section via two tubes (C). Flow passes through the glass spheres (D) where some of the turbulence is killed. After that, honeycomb (E) helps to straighten the flow. Flow is then forced through a set of screens (F) to decrease the turbulence level again. Contraction (G) accelerates the flow before the exit section. [22]

be performed, detecting the separation point and recirculation bubbles. Inlet conditions (like blockage factor or turbulence intensity) can be changed by inserting a channel of variable length between the wind tunnel effuser outlet and diffuser inlet.

To assess the validity of the RANS model, simulations on 2D diffusers can be performed, starting from inlet conditions directly acquired by using hot-wire anemometers.

A possible setup is to utilise a planar jet wind tunnel to maintain a high aspect ratio to guarantee the two-dimension constraint. The following setup has been developed based on the planar jet wind tunnel available at the CICLoPE laboratory (University of Bologna), but the same concept can be adapted as needed.

As shown in Figure 5.1, this open-loop blowing wind tunnel was initially designed to calibrate hot-wire anemometers and to characterise the planar jet flow. As schematised, there is a three-phase AC motor that drives the fan which increases the pressure at the pre-settling chamber. The latter is used to dampen fluctuations caused by the fan. Once the flow enters the rectangular prism section, it encounters different devices that help to straighten the flow and decrease the turbulence level thanks to the strong pressure drops. In the end, the convergent part (contract ratio of 9:1) increases the velocity and laminarises the flow.

In order to analyse the different diffusers, a new convergent channel was designed, so that the end presents a flange that could be mounted in place of part G of Figure 5.1. The model was 3D-printed and the new contract ratio was increased to 19:1 in order to reduce the outlet width. The convergent channel was designed with a hyperbolic tangent shape in order to optimize the outlet flow and reduce the pressure losses. The convergent outlet is rectangular with fillets at the corners. Given W_1 the height of the outlet, the fillets are $1/10W_1$, with $W_1 = 20\ mm$. After the effuser, a channel of length $5W_1$ is flanged in order to homogenise the flow. After the channel, the different diffusers are flanged and they discharge directly in a stationary atmosphere (plenum exit condition). The aspect ratio (AS) of the diffusers is 10, in fact, the diffuser span width measures 200 mm. All the parts are 3D-printed and the assembly is illustrated in Figures 5.2 and 5.3.

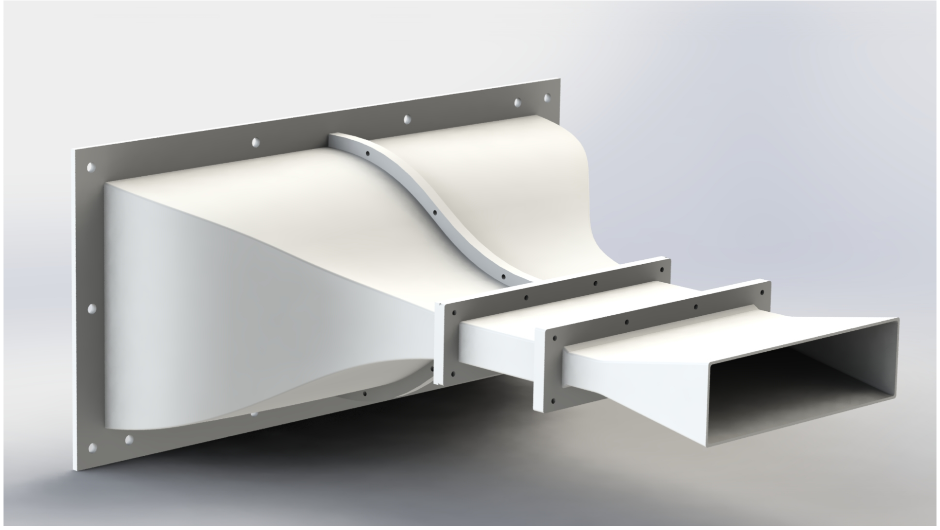

Figure 5.2: Render of the assembly to be flanged on the planar jet wind tunnel of Figure 5.1 to test the different diffusers.

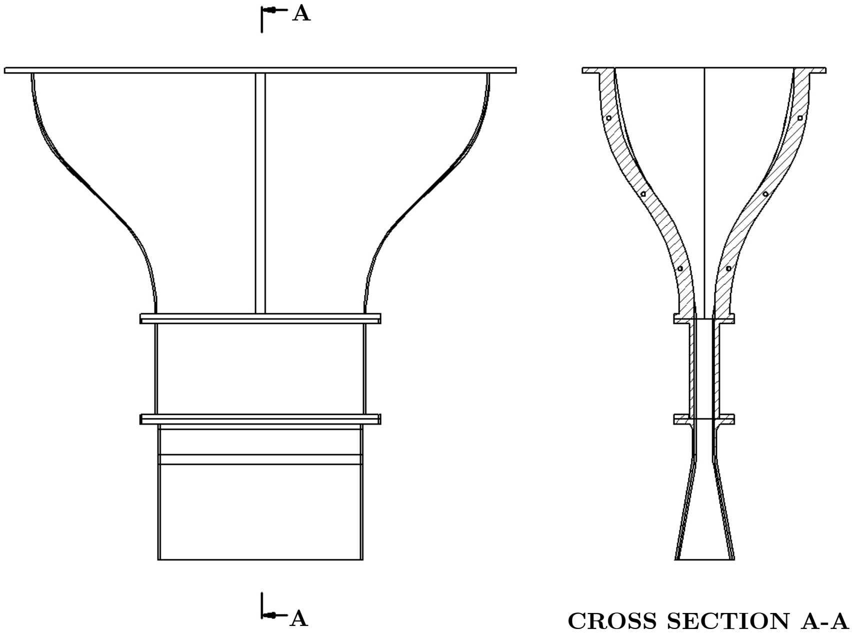

Figure 5.3: Cross section of the assembly of Figure 5.2.

Bibliography

[1] Stephen Jay Kline et al. “Optimum design of straight-walled diffusers”. In: *Journal of Basic Engineering* 81.3 (1959), pp. 321–329.

[2] Leon Ross Reneau et al. “Performance and design of straight, two-dimensional diffusers”. In: (1967).

[3] Arvind Shreedhar Dighe. “Effects of aspect-ratio and low Reynolds number on the pressure recovery and flow regime behavior of plane wall diffusers”. PhD thesis. Purdue University, 1973.

[4] Guido Buresti. *Elements of fluid dynamics*. Vol. 3. World Scientific Publishing Company, 2012.

[5] Steven J Daniels et al. “Automated shape optimisation of a plane asymmetric diffuser using combined Computational Fluid Dynamic simulations and multi-objective Bayesian methodology”. In: *International Journal of Computational Fluid Dynamics* 33.6-7 (2019), pp. 256–271.

[6] Michael Casey and Chris Robinson. *Radial Flow Turbocompressors: Design, Analysis, and Applications*. Cambridge University Press, 2021. DOI: `10.1017/9781108241663`.

[7] J Ashjaee and JP Johnston. “Straight-walled, two-dimensional diffusers—transitory stall and peak pressure recovery”. In: (1980).

[8] DJ Cockrell and E Markland. “A Review of Incompressible Diffuser Flow: A Reappraisal of an Article by GN Patterson entitled ‘Modern Diffuser Design’which was published in this journal twenty-five years ago”. In: *Aircraft Engineering and Aerospace Technology* 35.10 (1963), pp. 286–292.

[9] CR Smith Jr and Stephen Jay Kline. “An experimental investigation of the transitory stall regime in two-dimensional diffusers”. In: (1974).

[10] AHM Kwong and AP Dowling. “Unsteady flow in diffusers”. In: (1994).

[11] Osborne Reynolds. “IV. On the dynamical theory of incompressible viscous fluids and the determination of the criterion”. In: *Philosophical transactions of the royal society of london.(a.)* 186 (1895), pp. 123–164.

[12] Joseph Boussinesq. *Théorie analytique de la chaleur: mise en harmonie avec la thermodynamique et avec la théorie mécanique de la lumière.* Vol. 2. Gauthier-Villars, 1903.

[13] B.E. Launder and D.B. Spalding. “The numerical computation of turbulent flows”. In: *Computer Methods in Applied Mechanics and Engineering* 3.2 (1974), pp. 269–289. ISSN: 0045-7825. DOI: https://doi.org/10.1016/0045-7825(74)90029-2. URL: https://www.sciencedirect.com/science/article/pii/0045782574900292.

[14] David C Wilcox. “Formulation of the kw turbulence model revisited”. In: *AIAA journal* 46.11 (2008), pp. 2823–2838.

[15] Florian R Menter. “Two-equation eddy-viscosity turbulence models for engineering applications”. In: *AIAA journal* 32.8 (1994), pp. 1598–1605.

[16] Florian R Menter et al. “Transition modelling for general purpose CFD codes”. In: *Flow, turbulence and combustion* 77 (2006), pp. 277–303.

[17] Robin B Langtry and Florian R Menter. “Correlation-based transition modeling for unstructured parallelized computational fluid dynamics codes”. In: *AIAA journal* 47.12 (2009), pp. 2894–2906.

[18] EM Sparrow et al. “Flow separation in a diverging conical duct: Effect of Reynolds number and divergence angle”. In: *International Journal of Heat and Mass Transfer* 52.13-14 (2009), pp. 3079–3083.

[19] Masaki Sano and Keiichi Tamai. “A universal transition to turbulence in channel flow”. In: *Nature Physics* 12.3 (2016), pp. 249–253.

[20] Amgad Salama. “Velocity profile representation for fully developed turbulent flows in pipes: a modified power law”. In: *Fluids* 6.10 (2021), p. 369.

[21] RA t Tyler and RG Williamson. “Paper 11: Diffuser Performance with Distorted Inflow”. In: *Proceedings of the Institution of Mechanical Engineers, Conference Proceedings*. Vol. 182. 4. SAGE Publications Sage UK: London, England. 1967, pp. 115–125.

[22] Mehmet Berkay Eryildiz. “Development and Automatization of a Planar Jet Wind Tunnel for the X-wire Calibration”. URL: `http://amslaurea.unibo.it/26985/`.